Dynamical and energetic instabilities in multicomponent Bose-Einstein condensates in optical lattices

J. Ruostekoski[1] and Zachary Dutton[2]

[1]*School of Mathematics, University of Southampton, Southampton, SO17 1BJ, United Kingdom*
[2]*Naval Research Laboratory, Washington, DC 20375, USA*
(Received 11 July 2007; published 10 December 2007)

We study dynamical and energetic instabilities in the transport properties of Bloch waves for atomic multi-component Bose-Einstein condensates in optical lattices in the tight-binding limit. We obtain stability criteria analytically, as a function of superfluid velocities and interaction parameters, in several cases, for two-component and spinor condensates. In the two-species case we find that the presence of the other condensate component can stabilize the superfluid flow of an otherwise unstable condensate and that the free space dynamical miscibility condition of the two species can be reversed by tuning the superfluid flow velocities. In spin-1 condensates, we find the steady-state Bloch wave solutions and characterize their stability criteria. We find that generally more regions of dynamical instability arise for the polar than for the ferromagnetic solutions. In the presence of magnetic Zeeman shifts, we find a richer variety of condensate solutions and find that the linear Zeeman shift can stabilize the superfluid flow in several cases of interest.

I. INTRODUCTION

There has been considerable recent interest in the dynamical properties of atomic Bose-Einstein condensates (BECs) in optical lattice potentials [1–16]. In optical lattices the nonlinear mean-field interaction of the BEC may give rise to dynamical and energetic instabilities in the transport properties of the atoms. For a single-component condensate, when the center-of-mass velocity reaches a critical value, the BEC dynamics become unstable, resulting in an abrupt stop of the transport of the atom cloud in the lattice. Such a superfluid to insulator transition has a classical nature and it can be described using the Gross-Pitaevskii (GP) mean-field models [12–14,16]. In the dynamically unstable regime, small initial perturbations around a moving solution grow exponentially in time, resulting in the randomization of the relative phases between atoms in adjacent lattice sites. The dynamical transition to inhibited atom transport was experimentally observed in the classical regime [2,5–8] and experimental methods to characterize both the dynamical and energetic instabilities of moving condensates have been developed [8]. Inhibition of transport was also observed in the presence of large quantum fluctuations using strongly confined narrow atom tubes [9]. In a confined system with enhanced quantum fluctuations the sharp classical transition is smeared out [17–19], resulting in a gradually increasing friction in the atom transport. Due to the broadening of the velocity distribution of the atoms, even at low velocities a non-negligible atom population occupies the dynamically unstable high-velocity region of the corresponding classical system, generating the friction in the studied case in the shallow lattice limit [18,20].

Despite this work on single-component condensates, there have been relatively few studies of dynamics of multicomponent BECs in optical lattices. Due to nearly equal trapping potentials of different Zeeman sublevels (for example, $F=1$, $m_F=-1$ and $F=2$, $m_F=1$ in ^{23}Na and ^{87}Rb), it is possible to create long-lived two-component BECs, forming an effective

spin-1/2 system. These have especially long lifetimes in ^{87}Rb due to a fortuitous cancellation of scattering lengths [21]. This additional degree of freedom has been utilized to study an interesting array of effects in both Bose-condensed and noncondensed cold Bose systems, including phase separation [22], optically induced shock waves [23], spin waves [24,25], overlapping ^{41}K-^{87}Rb BEC mixtures [26], spin squeezing [27], and vector soliton structures [28–30]. Experimental work on two-component BECs in optical lattices, from the viewpoint of quantum logic gates, was reported in [31]. There has also been a recent experimental realization of a two-species ^{41}K-^{87}Rb Bose mixture in an optical lattice [32].

Alternatively, in dipole traps [33] the spin of the atom is no longer constrained by the magnetic field and, due to the additional atomic spin degrees of freedom, the BEC exhibits a richer spinor order parameter structure. The spin of the optically trapped BECs can generally have significant effects on the dynamical properties of the BECs [33,34], give rise to spin textures [35], and support highly nontrivial defect structures [36–39]. Experiments have also explored dynamics in spinor condensates in harmonic traps [40–43] and optical lattices [44], and the application of spinor gases to spatially resolved magnetometry [45].

In this paper, we investigate both dynamical and energetic instabilities in the transport of multicomponent BECs in optical lattices. We first consider magnetically trapped two-component BECs where the two condensates occupy different hyperfine states of the same atom or are formed by mixtures of two different atoms. Transport properties of two-component BECs in an optical lattice were studied in Ref. [46], and numerical results for dynamical instabilities were presented for a special case. In particular, dynamical instabilities were shown to arise from the critical velocity as well as from the phase separation of the two species. In contrast to that work, we obtain analytic results for the condensate dynamical instability points and analyze in detail the complete phase space of stability criteria for both dynamical and en-

ergetic instabilities across a broad range of parameters. We vary the intra- and interspecies interaction strengths, the site hopping term for each spin component independently, as well as the velocities of the two BECs, allowing application of our results to a large variety of experimental systems. In contrast to Ref. [46], we find the possibility of a second BEC component stabilizing the superfluid flow of an otherwise unstable first BEC component (which exceeds the critical velocity of a single-component BEC). In addition, we find that the free space phase separation criterion, that the square of the interspecies interaction coefficient exceeds the product of the intraspecies interaction coefficients ($U_{12}^2 > U_{11}U_{22}$), can be reversed in an optical lattice. This can happen if one of the BECs has a velocity larger and the other one smaller than the single-species critical velocity (the effective masses of the two components exhibit different signs).

We also analyze transport properties of optically trapped spin-1 BECs in optical lattices, which have not been experimentally investigated to date. Here we obtain analytic expressions for both the dynamical and energetic instability regions of the Bloch wave solutions. In contrast to the two-component case, spin-changing collisions allow the atom population of different spin components to adjust to lower the energy of the system, according to whether the scattering lengths correspond to polar or ferromagnetic values. Our results illuminate the different stability properties of the polar versus ferromagnetic solutions, which, in the absence of Zeeman shifts, are most apparent for large spin-dependent scattering lengths or when the spin-dependent and spin-independent scattering lengths exhibit different signs. The presence of the Zeeman level shifts provides a richer variety of steady-state Bloch wave solutions, including a new set of solutions that do not exist for the case of small level shifts. We find that the quadratic Zeeman shift, due to its role in the energy conservation of spin-changing collisions, plays an important role in the stability of various condensate solutions. However, we also see that linear Zeeman shifts play an important role in stabilizing many of the solutions. The dynamical instabilities of the spinor BECs can be important, e.g., also in the formation of solitons, which have been studied in the homogeneous case in Ref. [47].

In Sec. II we introduce the discrete nonlinear Schrödinger equation and the Bogoliubov–de Gennes approach to study the stability properties of condensate solutions. This is done in the context of the two-component case but the same method is used later for the spinor case. We then derive expressions for the normal mode energies and discuss the dynamical and energetic stability of the two-component case. In Sec. III we apply this method to the spinor case. We first discuss the polar case, then the ferromagnetic case, and then finally the effect of the Zeeman shifts. Some experimental considerations for observation of the effects studied are discussed in Sec. IV. We summarize our results in Sec. V. The Bogoliubov–de Gennes matrices are presented explicitly in Appendix A and the detailed analysis of the stability of the two-component case when the phase separation condition is reversed is given in Appendix B.

II. A TWO-COMPONENT CONDENSATE IN AN OPTICAL LATTICE

A. Two-species system description

Two-component BECs can be prepared in magnetic traps by simultaneously confining different atomic species in the same trap. The atoms may occupy two different hyperfine states of the same atomic species or form a mixture of two condensates of two different atomic species. For instance, two BEC components in perfectly overlapping isotropic magnetic trapping potentials were experimentally realized in hyperfine spin states of ^{87}Rb, $|\uparrow\rangle \equiv |F=2, m_f=1\rangle$ and $|\downarrow\rangle \equiv |F=1, m_f=-1\rangle$. In this system the inter- ($a_{\uparrow\downarrow}$) and intraspecies ($a_{\uparrow\uparrow}$ and $a_{\downarrow\downarrow}$) interaction strengths are nearly equal, with $a_{\downarrow\downarrow}:a_{\uparrow\downarrow}:a_{\uparrow\uparrow}::1.024:1:0.973$ [48]. Since the scattering lengths satisfy $a_{\uparrow\downarrow}^2 \gtrsim a_{\uparrow\uparrow}a_{\downarrow\downarrow}$, the two species experience dynamical phase separation and can strongly repel each other [22]. A more strongly repelling two-component system of different species was created using a ^{41}K-^{87}Rb mixture [26]. The interatomic interactions of two magnetically trapped BEC components do not mix the atom population, and the atom numbers of both species are separately conserved.

The dynamics of the BECs follow from the coupled Gross-Pitaevskii equation (GPE)

$$i\hbar \frac{\partial \psi_j}{\partial t} = \left(-\frac{\hbar^2}{2m_j}\nabla^2 + V_j(\mathbf{r}) + \sum_k \kappa_{jk}|\psi_k|^2 \right)\psi_j. \quad (1)$$

Here we have defined the interaction coefficients $\kappa_{ii} \equiv 4\pi\hbar^2 a_{ii}/m_i$ and $\kappa_{ij} \equiv 2\pi\hbar^2 a_{ij}/\mu$ ($i \neq j$), where the wave functions are normalized to N_j, $N=N_1+N_2$ is the total atom number, m_j is the atomic mass of BEC component $|j\rangle$, and $\mu = m_1 m_2/(m_1+m_2)$ is the reduced mass. The intraspecies and interspecies scattering lengths are denoted by a_{ii} and a_{ij} ($i \neq j$), respectively. The external potential is generally a superposition of a harmonic trapping potential $V_H^{(j)}(\mathbf{r}) = m(\omega_{jx}^2 x^2 + \omega_{jy}^2 y^2 + \omega_{jz}^2 z^2)/2$ and the periodic optical lattice potential $V_L^{(j)}(\mathbf{r}) = V_0^{(j)}\sin^2(\pi x/a + \varphi_j)$, $V_j(\mathbf{r}) = V_H^{(j)}(\mathbf{r}) + V_L^{(j)}(\mathbf{r})$, where a denotes the lattice spacing. In the following we ignore the effect of the harmonic trapping potential along the lattice and consider the system as translationally invariant. We also neglect density fluctuations orthogonal to the optical lattice and consider the dynamics as effectively one dimensional (1D).

We write the GPE in the tight-binding approximation by expanding the BEC wave functions on the basis of the Wannier functions and only keep the lowest vibrational states in each lattice site η, so that $\psi_j(\mathbf{r}) = \sum_\eta c_\eta^{(j)}\phi_{j\eta}(\mathbf{r})$ [49]. We obtain discrete nonlinear Schrödinger equations (DNLSEs):

$$i\hbar \frac{dc_\eta^{(j)}}{dt} = -J_j(c_{\eta+1}^{(j)} + c_{\eta-1}^{(j)}) + \sum_k U_{jk}|c_\eta^{(k)}|^2 c_\eta^{(j)}. \quad (2)$$

With similar assumptions, we have the hopping amplitude $J_j > 0$ for the atoms between adjacent lattice sites:

$$J_j \simeq -\int d^3r \left(\frac{\hbar^2}{2m_j}\boldsymbol{\nabla}\phi_{j\eta}^* \cdot \boldsymbol{\nabla}\phi_{j,\eta+1} + \phi_{j\eta}^* V_L^{(j)}\phi_{j,\eta+1} \right). \quad (3)$$

The nonlinearities are given by $U_{jk} \simeq \kappa_{jk}\int d^3r|\phi_{j\eta}|^2|\phi_{k\eta}|^2$. The two BEC species may generally experience different lat-
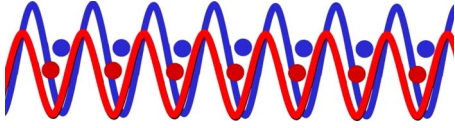
FIG. 1. (Color online) The two BECs may experience different optical lattice potentials that can be shifted with respect to each other. The interspecies interaction strength U_{12} is proportional to the overlap integral of the two lattice site mode functions and it can be adjusted by shifting the lattices. Moreover, the kinetic energy hopping amplitude of the two species J_1, J_2 may be independently modified by changing the barrier height between the neighboring sites.

tice potentials [31] and so the interspecies coupling coefficient U_{12} may be varied by displacing the two lattice potentials with respect to each other (to modify the overlap integral between the wave functions), even when the values of the scattering lengths remain constant (Fig. 1).

B. Dynamical stability of two species

1. Collective two-component excitations

We study the stability of plane wave solutions to Eq. (2) by investigating the effect of small perturbations around the carrier wave. Our treatment is analogous to the approach in Ref. [13] to analyze single-component BECs. For the constant atom density along the lattice, the Bloch waves $c_\eta^{(j)} = \sqrt{n_j} \exp[i(k_j a \eta - \nu_j t)]$ that satisfy Eq. (2) exhibit the frequency $\nu_j = \Sigma_i n_i U_{ji} - 2J_j \cos(k_j a)$, where $n_j = |c_\eta^{(j)}|^2$ denotes the constant atom population in spin state j at each site. The perturbed carrier wave can be written as a Bogoliubov expansion:

$$c_\eta^{(j)} = (\sqrt{n_j} + u_j e^{iqa\eta} - v_j^* e^{-iqa\eta}) e^{i(k_j a\eta - \nu_j t)}. \tag{4}$$

Here the k_j represent the potentially nonzero velocities of the condensate in each component j. The stability of such states in a single-component BEC has been studied experimentally in Refs. [7,8] by dynamically moving the lattice potential. Substituting this expansion into Eq. (2) and linearizing the equations in u_1, v_1, u_2, and v_2 yield a system of four equations

$$i\frac{d}{dt}\mathbf{x} = \sigma \mathcal{M}(q)\mathbf{x}, \quad \mathbf{x} = \begin{pmatrix} u_1 \\ v_1 \\ u_2 \\ v_2 \end{pmatrix}, \quad \sigma = \begin{pmatrix} \sigma_z & 0 \\ 0 & \sigma_z \end{pmatrix}, \tag{5}$$

where σ_z denotes the 2×2 Pauli spin matrix. The elements of the 4×4 matrix $\mathcal{M}(q)$ follow from the linearization procedure as in the single-component BEC case. We write out this matrix explicitly in Appendix A. The eigenvalue problem for the matrix $\sigma\mathcal{M}(q)$ can be solved analytically. In order to preserve the symmetry properties of the Bogoliubov equations and to obtain simple analytic expressions for the normal mode energies we require that the atom currents of the two BECs are equal, i.e., $J_1 \sin(k_1 a) = J_2 \sin(k_2 a)$.

The eigenvalues represent the normal mode energies and read

$$\omega_q = 2J_1 \sin(k_1 a)\sin(qa) \pm \sqrt{\frac{1}{2}(\omega_{1,q}^2 + \omega_{2,q}^2) \pm \frac{1}{2}\sqrt{(\omega_{1,q}^2 - \omega_{2,q}^2)^2 + 16\epsilon_{1,q}\cos(k_1 a)\epsilon_{2,q}\cos(k_2 a)n_1 n_2 U_{12}^2}}. \tag{6}$$

The four eigenvalues correspond to all permutations of the $\pm$ signs. Only two of the eigenvalues are independent. The first term in Eq. (6) represents the Doppler shift of the excitation energies due to the superfluid current. Here $\omega_{j,q}$ denotes the single-condensate normal mode energies (without the Doppler shift term)

$$\omega_{j,q}^2 = \epsilon_{j,q}\cos(k_j a)[\epsilon_{j,q}\cos(k_j a) + 2n_j U_{jj}], \tag{7}$$

and

$$\epsilon_{j,q} = 4J_j \sin^2\left(\frac{qa}{2}\right) \tag{8}$$

is the spectrum of an ideal, nonmoving BEC.

For the case of positive definite $\mathcal{M}(q)$ all the eigenvalues ω_q of $\sigma\mathcal{M}(q)$ are real. In that case the physical solutions of the corresponding eigenvectors $\mathbf{y}$ exhibit positive normalization $\mathbf{y}^\dagger \sigma \mathbf{y} = 1$ (the $+$ sign in the front of the first square root) and unphysical eigenvectors negative normalization $\mathbf{y}^\dagger \sigma \mathbf{y} = -1$ (the $-$ sign in the front of the first square root). The eigenvalues ω_q with a nonvanishing imaginary part are associated with eigenvectors satisfying $\mathbf{y}^\dagger \sigma \mathbf{y} = 0$. The BEC system becomes dynamically unstable when the normal mode frequencies in Eq. (6) exhibit nonvanishing imaginary parts, indicating perturbations that grow exponentially in time. Such modulational instabilities occur in a closed system due to the nonlinear dynamics and do not require energy dissipation. The rate at which the instability sets in depends on the magnitude of the imaginary part of the eigenfrequency.

For small momenta, $qa \ll 1$, $\epsilon_{j,q} \simeq J_j q^2 a^2 = \hbar^2 q^2 / 2m_j^*$, where we introduced the effective mass of a noninteracting BEC as $m_j^* = \hbar^2 / (2J_j a^2)$. Similarly, we obtain $2J_1 \sin(k_1 a)\sin(qa) \simeq 2J_1 k_1 qa^2 = \hbar^2 k_1 q / m_1^*$ reinforcing the interpretation of the first term in Eq. (6) as the Doppler shift contribution.

If we set $U_{12} = 0$ in Eq. (6), we obtain independently the decoupled normal mode energies of the two BECs $\omega_q = 2J_1 \sin(k_1 a)\sin(qa) + |\omega_{1,q}|$ and $\omega_q = 2J_1 \sin(k_1 a)\sin(qa) + |\omega_{2,q}|$, analogously to the single-condensate normal modes obtained in Ref. [13].

The intraspecies interaction U_{12} mixes the normal modes of the two BECs. In the experimentally interesting regime $n_j U_{jj} \gg J_j$, if $U_{12}^2 \simeq U_{11} U_{22}$, one of the frequencies approaches zero indicating an instability similar to the uniform two-component BEC system. Specifically, for $k_1 = k_2 = 0$, we obtain in that case $\omega_{q,+}^2 \simeq \omega_{1,q}^2 + \omega_{2,q}^2$ and $\omega_{q,-}^2 \ll \omega_{1,q}^2, \omega_{2,q}^2$.

By expanding ω_q for small q in Eq. (6) with $k_1 = k_2 = 0$, we obtain $\omega_q \simeq \hbar s q$ where s is the speed of sound

$$s_{\pm} = \frac{a}{\hbar} \sqrt{J_1 n_1 U_{11} + J_2 n_2 U_{22} \pm \sqrt{(J_1 n_1 U_{11} - J_2 n_2 U_{22})^2 + 4 J_1 J_2 n_1 n_2 U_{12}^2}}. \tag{9}$$

The long wavelength excitations are unstable when one of the solutions for the speed of sound has an imaginary part.

If we do not assume that the two BEC currents are equal, $J_1 \sin(k_1 a) \neq J_2 \sin(k_2 a)$, the Doppler shifts for the two BECs are different and the usual symmetry properties between the positive and the negative energy Bogoliubov eigenfunctions are lost. We still find analytic solutions for the eigenenergies ω_q, but these no longer have simple compact expressions as in Eq. (6). The basic formalism may be used to generate stability diagrams in these cases numerically, for instance, even if the two BECs have velocities in the opposite directions. In the following we concentrate on analyzing the general features of the two-component system that may already be obtained from Eq. (6).

2. Stability with equal signs for cos(k₁a) and cos(k₂a)

We first analyze the dynamical stability of the two-component system, given in Eq. (6) for $J_1 \sin(k_1 a) = J_2 \sin(k_2 a)$, for the case that $\cos(k_1 a)$ and $\cos(k_2 a)$ exhibit equal sign. We find two different inequalities can cause instabilities in this case.

The first occurs when $\omega_{1,q}^2 + \omega_{2,q}^2 < 0$, which makes the expression inside the square root in Eq. (6) negative (for any values of U_{12}). Physically, this corresponds to the situation where the two-component dynamical instability is driven by the instabilities of the individual single-component BEC excitations (7). We have $\omega_{1,q}^2 + \omega_{2,q}^2 < 0$, for some values of q, if

$$\sin^2\left(\frac{qa}{2}\right) < -\frac{D_{11} + D_{22}}{2[J_1^2 \cos^2(k_1 a) + J_2^2 \cos^2(k_2 a)]}, \tag{10}$$

where

$$D_{ij} = J_i \cos(k_i a) n_j U_{jj}. \tag{11}$$

The inequality is most easily satisfied for excitations in the long-wavelength limit $q \to 0$, and is satisfied when the right-hand side is positive, i.e., for

$$D_{11} + D_{22} < 0. \tag{12}$$

In particular, for $U_{11}, U_{22} > 0$ we find that, according to Eq. (12), the modes are unstable if $k_1 a, k_2 a > \pi/2$. In this case, the instability is analogous to the high-velocity instability seen in the single-component case [12].

A second kind of instability occurs for some particular values of U_{12} when $\omega_{1,q}^2 + \omega_{2,q}^2 \geq 0$. We find that this instability corresponds to the phase separation phenomena which occur in the two-component free space case [22]. In particular, the two-component system in Eq. (6) is always dynamically unstable [for the case that $\cos(k_1 a)$ and $\cos(k_2 a)$ exhibit equal sign] if

$$U_{12}^2 > U_{11} U_{22}, \tag{13}$$

as the expression in the outer square root in Eq. (6) becomes negative. The particular unstable q modes are those that satisfy (when $\omega_{1,q}^2 + \omega_{2,q}^2 \geq 0$)

$$\sin^2\left(\frac{qa}{2}\right) < \frac{-(D_{12} + D_{21}) + \sqrt{(D_{12} - D_{21})^2 + 4 J_1 \cos(k_1 a) J_2 \cos(k_2 a) n_1 n_2 U_{12}^2}}{4 J_1 \cos(k_1 a) J_2 \cos(k_2 a)}. \tag{14}$$

While the unstable dynamics for $U_{12}^2 > U_{11} U_{22}$ correspond to the analogous instability in the free space, one should emphasize that the value of U_{12} is determined not only by the interspecies scattering length, but also by the spatial overlap integral of the lattice site wave functions for the two species; see the definition of U_{ij} below Eq. (3). By means of shifting the relative position of the two BEC lattice potentials, one may easily reduce the value of U_{12}.

Thus the two-component system must satisfy $J_1 \cos(k_1 a) n_1 U_{11} + J_2 \cos(k_2 a) n_2 U_{22} > 0$ and $U_{12}^2 \leq U_{11} U_{22}$ to be dynamically stable. In the case that $\cos(k_1 a)$ and $\cos(k_2 a)$ exhibit the same sign, the first condition implies $k_1 a, k_2 a < \pi/2$ for $U_{11}, U_{22} > 0$ or $k_1 a, k_2 a > \pi/2$ for $U_{11}, U_{22} < 0$. In this case if U_{11}, U_{22} exhibit the opposite signs, the system is unstable even if Eq. (12) is not satisfied, since $U_{12}^2 > U_{11} U_{22}$.

Phase space diagrams of the dynamical instability strengths as a function of the excitation wavelength q and condensate wave number k are shown in Fig. 2. In Fig. 2(a)
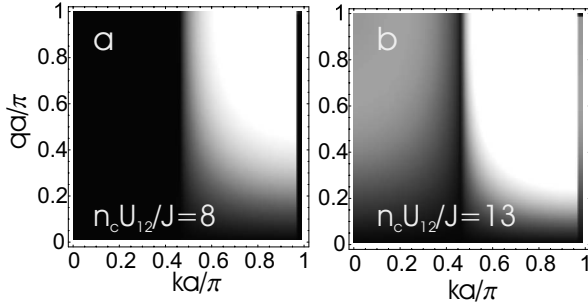
FIG. 2. (a) Largest imaginary part of the eigenvalues Eq. (6) as function of $k \equiv k_1 = k_2$ and q for the case $n_1 U_{11} = n_2 U_{22}$, $n_c U_{12} = 8J_1$, and $J_2 = J_1$. We define $n_c \equiv \sqrt{n_1 n_2}$. Gray scale goes from 0 (black) to $5J_1$ (white). (b) Same plot with $n_c U_{12} = 13J_1$ (phase separation regime).

we see that the system is stable for the case $n_c U_{12} = 8J_1$, $n_1 U_{11} = n_2 U_{22} = 10J_1$ (defining $n_c = \sqrt{n_1 n_2}$) when $ka < 0.5\pi$, and then becomes unstable for $ka > 0.5\pi$, in accordance with Eq. (12). The strengths of the instabilities (the largest imaginary part of the eigenvalues) are linear in q [for the slope, see Eq. (9)] until they saturate approximately at a value $\mathrm{Im}(\omega_q) \simeq \sqrt{-16 n_c U_{12} J_1 \cos(k_1 a)}$, which is $\approx 11J_1$ at $ka = \pi$ in Fig. 2(a). The strongest instability at $ka = \pi$ represents period doubling that drives the system away from the Bloch state. The behavior is qualitatively similar for all $n_c U_{12} \lesssim n_1 U_{11} = n_2 U_{22}$ and also for smaller values of J_1 and J_2. However, for $n_c U_{12} > n_1 U_{11}$ [Fig. 2(b)], we see that the predicted phase separation instability arises in the $ka < 0.5\pi$ region. It is interesting to note that this instability is markedly weaker than the high-velocity instability ($ka > 0.5\pi$), as its maximum value (occurring for $k = 0$, $qa = \pi$) scales as $\mathrm{Im}(\omega_q) \simeq \sqrt{8(n_c U_{12} - n_1 U_{11}) J_1}$ (in the limit that $n_c U_{12} - n_1 U_{11} \gg J_1$). In the case plotted in Fig. 2(b), the value saturates at $\approx 3J_1$, whereas the instability strength in the $ka > 0.5\pi$ region reaches $\approx 13J_1$.

Figures 3(a) and 3(b) compare the phase separation instability versus $n_c U_{12}$ for $k_1 a = k_2 a = 0$ and $k_1 a = k_2 a = 0.4\pi$. Generally speaking, the largest imaginary value reaches a maximum value $\mathrm{Im}(\omega_q) \simeq \sqrt{8(n_c U_{12} - n_1 U_{11}) J_1}$. The dependence on the sign of U_{11}, U_{22} is shown in Fig. 4. We see in Fig. 4(a) that, for $n_c U_{12} < n_1 U_{11} = n_2 U_{22}$ and $\cos(k_1 a) > 0$, the instability is restricted to the attractive cases $U_{11} < 0$. Figure 4(b) demonstrates that this instability switches to the repulsive case for $\cos(k_1 a) < 0$. Again these instabilities reach strengths $\mathrm{Im}(\omega_q) \simeq \sqrt{16 n_1 U_{11} J_1}$. However, for the $\cos(k_1 a) < 0$ case, there occurs also a much weaker instability for attractive interactions with strength $\mathrm{Im}(\omega_q) \simeq \sqrt{8(n_c U_{12} - n_1 U_{11}) J_1}$.

3. Stability with different signs for $\cos(k_1 a)$ and $\cos(k_2 a)$

The case that $\cos k_1 a$ and $\cos k_2 a$ have different signs represents a configuration where the velocities of the two BECs are located on the opposite sides of the deflection point in the ideal, single-particle BEC excitation spectrum (8) (the effective masses of the two components exhibit different signs) and is presented in detail in Appendix B. In that
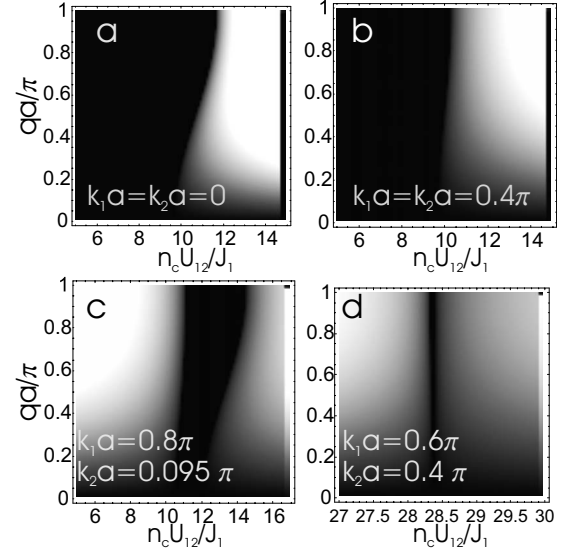

FIG. 3. (a),(b) Imaginary part of the eigenvalues versus $n_c U_{12}$ (again $n_c = \sqrt{n_1 n_2}$), holding $n_1 U_{11} = n_2 U_{22} = 10J_1$ for the indicated condensate velocities k. Here $J_2 = J_1$. (c) A case with opposite signs of $\cos(k_1 a)$ and $\cos(k_2 a)$, showing a region of dynamical stability for all q. Here $n_1 U_{11} = 10J_1$, $n_2 U_{22} = 12J_1$, and $J_2 = 2J_1$. A similar narrow stable region exists around $n_c U_{12} \simeq -12J_1$. (d) Another case with opposite signs of $\cos(k_1 a)$ and $\cos(k_2 a)$. Here $n_1 U_{11} = 27J_1$, $n_2 U_{22} = 30J_1$, and $J_2 = J_1$. Again another stable region in this case is located close to $n_c U_{12} \simeq -28.5J_1$. In these plots the gray scale goes from 0 to $5J_1$.

situation, we also always find a dynamical instability when $\omega_{1,q}^2 + \omega_{2,q}^2 < 0$, resulting in the relation similar to Eq. (12). In this case, however, the high-velocity instability condition is highly nontrivial, depending on the values of the hopping amplitudes, interaction strengths, atom numbers, and velocities: One of the BECs that reaches the single-component critical velocity $k_1 a > \pi/2$ may, or may not, destabilize the two-component BEC system, depending on the parameter values. Moreover, for $\omega_{1,q}^2 + \omega_{2,q}^2 \geq 0$, the dynamical stability condition due to the phase separation of the nonmoving system, $U_{12}^2 < U_{11} U_{22}$, is reversed, so that the *entire* dynamically stable region occurs, when $U_{12}^2 > U_{11} U_{22}$. In particular, as shown in Appendix B, we find there is a band of values for U_{12} where the system is dynamically stable, defined by either
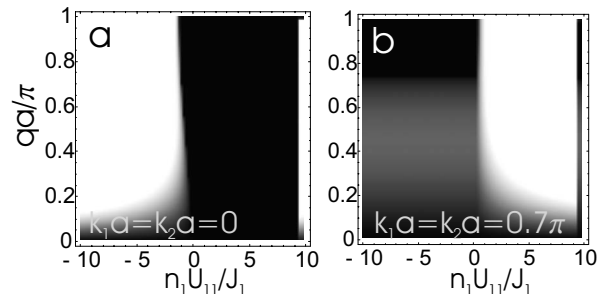

FIG. 4. Imaginary part of the eigenvalues versus q and varying $n_1 U_{11} = n_2 U_{22}$, keeping $n_c U_{12} = n_1 U_{11} - J_1$ and with $J_2 = J_1$. In this figure, the gray scale runs from 0 to $2.5J_1$.

$U_{11}U_{22} < U_{12}^2 < \xi_1$ or $U_{11}U_{22} < \xi_2 < U_{12}^2 < \xi_1$, depending on the value of U_{11}. Here ξ_1 and ξ_2 are defined in Eqs. (B4) and (B9). Interestingly, this also represents a situation where the other condensate component can stabilize the superfluid flow of an otherwise unstable condensate (exceeding the single-component critical velocity). Moreover, the two-component system may be dynamically stable even for $U_{11} < 0$ and $U_{22} > 0$, since in that case $U_{11}U_{22} < U_{12}^2$.

Figures 3(c) and 3(d) show cases with $\cos(k_1 a)$ and $\cos(k_2 a)$ of different signs [but satisfying the condition $J_1 \sin(k_1 a) = J_2 \sin(k_2 a)$]. For the parameters of Fig. 3(c) there is a range of $n_c U_{12}$ for which the system is dynamically stable. In this case $n_1 U_{11}$ satisfies Eq. (B7) and the dynamically stable region, according to Eq. (B8), is $\xi_2 \leq U_{12}^2 < \xi_1$. The relevant quantities are $n_c\sqrt{\zeta_2} = 11.5 J_1$ and $n_c\sqrt{\zeta_1} = 12.5 J_1$ for this example. Note that the dynamical instabilities tend to be much weaker on the large-U_{12} side of this stability range. In Fig. 3(c) we have different hopping amplitudes $J_1 \neq J_2$. Figure 3(d) shows a case with a smaller range of stable $n_c U_{12}$ but with $J_1 = J_2$. In this case $n_1 U_{11}$ satisfies Eq. (B5) and the dynamically stable region, according to Eq. (B6), is for $U_{11}U_{22} < U_{12}^2 < \xi_1$. Here $n_c\sqrt{U_{11}U_{22}} = 28.46 J_1$ and $n_c\sqrt{\zeta_1} = 28.50 J_1$.

C. Energetic stability

The energetic stability of the superfluid flow of the homogeneous two-component mixture depends on the properties of the energy functional. The second-order variations of the energy for small perturbations in the carrier wave are determined by the matrix $\mathcal{M}(q)$ and the system is energetically stable if $\mathcal{M}(q)$ is positive definite. If any of the eigenvalues of $\mathcal{M}(q)$ are negative, the system may relax to a state with lower energy by means of dissipative coupling to the environment. The rate at which such relaxation happens depends on the strength of the coupling, e.g., on the number of thermal atoms interacting with the condensate.

The eigenvalues of $\mathcal{M}(q)$ can also be evaluated analytically but the full solutions are rather lengthy. In Fig. 5 we show the energetically unstable regions of the two-component dynamics. Note that positive definite $\mathcal{M}(q)$ implies real eigenvalues ω_q of $\sigma\mathcal{M}(q)$ in Eq. (6), so the dynamically unstable region always forms a subset of the energetically unstable region. Figures 5(a) and 5(b) show cases with $n_c U_{12} < n_1 U_{11}$ and $n_c U_{12} > n_1 U_{11}$, respectively. In the latter case there are regions of instability for some q at all condensate wave numbers k. In the former case, there are is a band of k with all q modes energetically stable, with a width proportional to $\sqrt{2J_1(n_1 U_{11} - n_c U_{12})}$, which determines the speed of sound for the spin wave; see Eq. (9) with $n_1 U_{11} = n_2 U_{22}$, $J_1 = J_2$. This is analogous to the single-component case [12] where there is a band of energetically stable k with a width proportional to the speed of sound proportional to $\sqrt{2J_1 n_1 U_{11}}$. In Figs. 5(c) and 5(d) we show the dependence on U_{12}. It is seen that at $k = 0$ instability occurs only for $U_{12} > U_{11}$ while for finite k the condition for stability becomes more stringent. For $ka > 0.5\pi$ the entire region is unstable. We also calculated that the specific parameter regimes corresponding to dynamical stability with
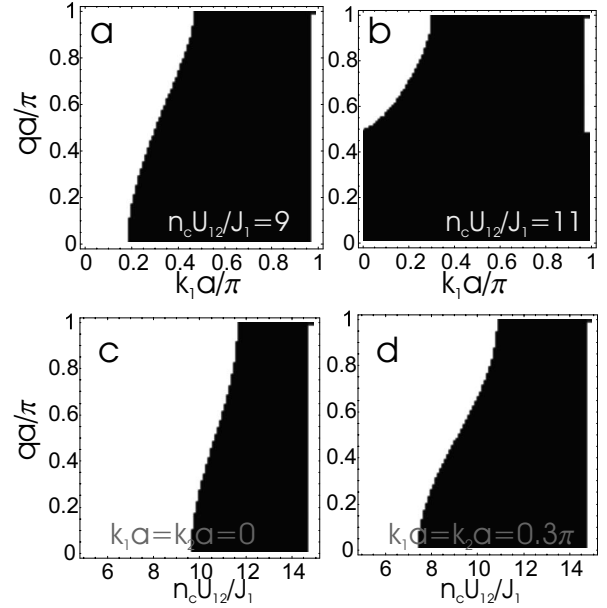

FIG. 5. (a), (b) Regions of energetic stability (white) and instability (black) versus k_1 and q for the cases indicated. We choose $n_1 U_{11} = n_2 U_{22} = 10 J_1$, $J_2 = J_1$, and $k_2 = k_1$. (c), (d) Energetic stability regions versus $n_c U_{12}$ for stationary and moving condensate cases.

two different condensate wave numbers k_1, k_2 [Figs. 3(c) and 3(d)] are energetically unstable at all q.

III. A SPIN-1 CONDENSATE IN AN OPTICAL LATTICE

A. Spinor Gross-Pitaevskii equations

We now consider a BEC of spin-1 atoms. In the absence of a magnetic trapping potential, the macroscopic BEC wave function is determined by a spinor wave function Ψ with three complex components [50]. The Hamiltonian density of the classical GP mean-field theory for this system reads:

$$\mathcal{H} = \frac{\hbar^2}{2m}|\nabla\Psi|^2 + V\rho + \frac{c_0}{2}\rho^2 + \frac{c_2\rho^2}{2}|\langle\mathbf{F}\rangle|^2 + g_1\langle\mathbf{B}\cdot\mathbf{F}\rangle\rho$$
$$+ g_2\langle(\mathbf{B}\cdot\mathbf{F})^2\rangle\rho. \tag{15}$$

In Eq. (15), $\mathbf{F}$ is the vector formed by the three components of the 3×3 Pauli spin-1 matrices [50], $\langle\mathbf{F}\rangle = \Psi^\dagger \cdot \mathbf{F} \cdot \Psi/\rho$ denotes the average spin, and $\rho(\mathbf{r}) = |\Psi(\mathbf{r})|^2$ the total atom density. The weak external magnetic field is denoted by $\mathbf{B}$ and is assumed to point along the z axis. The magnetic field produces linear and quadratic Zeeman level shifts whose effect is described by the last two terms in Eq. (15). As in the two-component case, the external potential V is the sum of the harmonic part V_H (in this case due to the optical dipole trap) and the optical lattice potential V_L: $V(\mathbf{r}) = V_H(\mathbf{r}) + V_L(\mathbf{r})$. In the following, we ignore the harmonic potential and, for simplicity, assume that the lattice potential is the same for all the spinor components. Thus the Wannier basis functions ϕ_η of our discrete basis no longer depend on the internal state j. Here c_0 and c_2 are the spin-independent and spin-dependent two-body interaction coefficients. In terms of

the s-wave scattering lengths a_0 and a_2, for the channels with total angular momentum zero and 2, they are $c_0 \equiv 4\pi\hbar^2(2a_2+a_0)/3m$ and $c_2 \equiv 4\pi\hbar^2(a_2-a_0)/3m$. For ^{23}Na, $(a_2-a_0)/3 \simeq 2a_B$ and $(2a_2+a_0)/3 \simeq 50a_B$, where $a_B = 0.0529$ nm is the Bohr radius [50], indicating $c_2/c_0 \simeq 0.04$. In contrast to the two-component case, in which the atom numbers in the two components do not mix, in the spinor case a homogeneous condensate wave function can adjust itself by varying the relative atom populations. From Eq. (15) in the absence of the external magnetic field we immediately observe that, since $c_2 > 0$ for ^{23}Na, corresponding to the *polar* phase, the energy is minimized by setting $\langle \mathbf{F} \rangle = \mathbf{0}$ throughout the BEC for the case of a uniform order parameter field. Alternatively, for ^{87}Rb we have $c_2/c_0 \simeq -0.0036$ [51]. The parameter values for ^{87}Rb correspond to the *ferromagnetic* phase, since $c_2 < 0$, and the energy in Eq. (15) in the absence of the external magnetic field is minimized when $|\langle \mathbf{F} \rangle| = 1$ throughout the BEC for the case of a uniform spin distribution.

Again using the lowest band of the Wannier state basis, the DNLSEs are written

$$i\hbar \frac{\partial c_\eta^{(+)}}{\partial t} = -J(c_{\eta+1}^{(+)} + c_{\eta-1}^{(+)}) + \delta_+ c_\eta^{(+)} + U_0 \sum_{\alpha=+,0,-} |c_\eta^{(\alpha)}|^2 c_\eta^{(+)}$$
$$+ U_2(|c_\eta^{(+)}|^2 - |c_\eta^{(-)}|^2 + |c_\eta^{(0)}|^2)c_\eta^{(+)} + U_2 c_\eta^{(-)*} c_\eta^{(0)2},$$

$$i\hbar \frac{\partial c_\eta^{(-)}}{\partial t} = -J(c_{\eta+1}^{(-)} + c_{\eta-1}^{(-)}) + \delta_- c_\eta^{(-)} + U_0 \sum_{\alpha=+,0,-} |c_\eta^{(\alpha)}|^2 c_\eta^{(-)}$$
$$+ U_2(|c_\eta^{(-)}|^2 - |c_\eta^{(+)}|^2 + |c_\eta^{(0)}|^2)c_\eta^{(-)} + U_2 c_\eta^{(+)*} c_\eta^{(0)2},$$

$$i\hbar \frac{\partial c_\eta^{(0)}}{\partial t} = -J(c_{\eta+1}^{(0)} + c_{\eta-1}^{(0)}) + U_0 \sum_{\alpha=+,0,-} |c_\eta^{(\alpha)}|^2 c_\eta^{(0)} + U_2(|c_\eta^{(+)}|^2$$
$$+ |c_\eta^{(-)}|^2)c_\eta^{(0)} + 2U_2 c_\eta^{(+)} c_\eta^{(-)} c_\eta^{(0)*}. \quad (16)$$

Here J is defined as before (3), but with no dependence on the internal state j [52] and $U_{0,2} \simeq c_{0,2} \int d^3r |\phi_\eta|^4$. The primary qualitative difference with the two-component case, seen in the last term of each of these equations, is the allowance of spin exchange collisions. The additional energy shift terms δ_+, δ_- account for Zeeman shifts (with respect to the level $m_F = 0$) due to an external magnetic field **B**. For simplicity, we ignore any effects of magnetic field gradients.

We study the stability of moving Bloch wave solutions to the DNLSEs (16). In order to find the low-energy stationary solutions, we substitute

$$\begin{pmatrix} c_\eta^{(+)} \\ c_\eta^{(0)} \\ c_\eta^{(-)} \end{pmatrix} = \begin{pmatrix} \zeta_+ \\ \zeta_0 \\ \zeta_- \end{pmatrix} \sqrt{n} \exp[i(ka\eta - \mu t)]. \quad (17)$$

Here μ is the chemical potential and $n = \sum_{\alpha=+,0,-} |c_\eta^{(\alpha)}|^2$ is the total condensate density that is assumed to be constant along the lattice. The spinor wave function $\vec{\zeta}^\dagger = (\zeta_+^*, \zeta_0^*, \zeta_-^*)$ satisfies the normalization condition $\vec{\zeta}^\dagger \cdot \vec{\zeta} = 1$. We concentrate on solutions for which $\vec{\zeta}$ is constant along the lattice.

We substitute the same Bogoliubov expansion as in Eq. (4) for the linearized fluctuations around the carrier wave solution (17) in the DNLSEs (16). This yields a 6×6 matrix $\sigma \mathcal{M}$, analogous to Eq. (5) (in this case with σ having three σ_z Pauli matrices in the diagonal), governing the dynamical stability of the system. The matrix $\mathcal{M}$ is given explicitly by Eq. (A2) in Appendix A.

As in the two-component BEC case, negative eigenvalues of the matrix $\mathcal{M}$ indicate the regions of energetic instability, while the eigenvalues of $\sigma \mathcal{M}$ yield the normal mode frequencies. The imaginary parts of these normal mode frequencies represent the strength of dynamical instabilities.

B. Stability in the polar case

1. Dynamical stability

In the polar case (that is energetically favored for $U_2 > 0$), we consider uniform spin profiles with the average spin value zero, and assume no Zeeman shifts for the time being $\delta_+ = \delta_- = 0$. All the degenerate, physically distinguishable, ground state solutions for $U_2 > 0$ may then be determined by means of the macroscopic BEC phase φ and a real unit vector **d** defining the quantization axis of the spin. The spinor wave function reads:

$$\begin{pmatrix} \zeta_+ \\ \zeta_0 \\ \zeta_- \end{pmatrix} = \frac{e^{i\varphi}}{\sqrt{2}} \begin{pmatrix} -d_x + id_y \\ \sqrt{2}d_z \\ d_x + id_y \end{pmatrix}. \quad (18)$$

As in the similar polar phase of superfluid ^{3}He-A [53], the states $(\mathbf{d}, \varphi)$ and $(-\mathbf{d}, \varphi + \pi)$ are identical. This can be conveniently taken into account by considering the **d** field to define unoriented axes rather than vectors.

The solution (17) with Eq. (18) has a chemical potential value $\mu = -2J\cos(ka) + U_0 n$ for any choice of $(\mathbf{d}, \varphi)$. Since also the excitations are the same for any values of $(\mathbf{d}, \varphi)$, we may choose the simplest form of the matrix $\mathcal{M}$ in Eq. (A2), which is obtained by choosing **d** to point along the z axis and $\varphi = 0$.

By calculating the eigenvalues of $\sigma \mathcal{M}$ with this particular choice of the BEC wave function we obtain analytic expressions for the normal mode energies

$$\omega_{1\pm}(q) = C_{q,k} \pm \sqrt{\epsilon_q \cos(ka)[\epsilon_q \cos(ka) + 2nU_0]},$$

$$\omega_{2\pm}(q) = C_{q,k} \pm \sqrt{\epsilon_q \cos(ka)[\epsilon_q \cos(ka) + 2nU_2]}, \quad (19)$$

where $\omega_{2\pm}$ are each doubly degenerate. The physical solutions correspond to the $+$ sign in the front of the square root. Here again ϵ_q denotes the spectrum of an ideal, nonmoving BEC

$$\epsilon_q = 4J\sin^2\left(\frac{qa}{2}\right), \quad (20)$$

and the Doppler shift term in the energy is given by

$$C_{q,k} = 2J\sin(qa)\sin(ka). \quad (21)$$

It is clear from Eq. (19) that, for $U_2 < U_0$ and $U_0 > 0$, $\omega_{1+}(q)$ drives the instability. The $\omega_{1+}(q)$ modes are unstable when
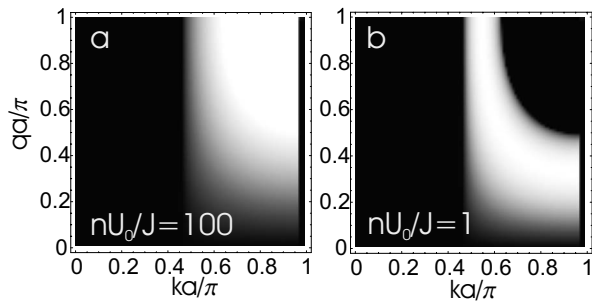
FIG. 6. (a) Largest imaginary part of the eigenvalues (19) versus k, holding $nU_0=100J$, $nU_2=4J$. Gray scale goes from 0 to $20J$. (b) A case with a weaker nonlinearity $nU_0=1J$, $nU_2=0.04J$ Gray scale goes from 0 to J.

the expression inside the square root is negative, which happens for q values that satisfy

$$\sin^2\left(\frac{qa}{2}\right) < -\frac{nU_0}{2J\cos(ka)}. \tag{22}$$

At least some modes are unstable whenever $ka > \pi/2$ and all the q modes are unstable when $-nU_0/(2J) < \cos(ka) < 0$. Figure 6(a) plots the largest imaginary part of the mode frequencies Eq. (19) versus q and k for the case $nU_0/J=100$ and $nU_2/J=4$ (corresponding to ^{23}Na). As in the two-component case, one sees the system is stable for $ka < \pi/2$, while for $ka > \pi/2$ one has an instability with a growth rate linear in q in the long-wavelength limit before saturating at a maximum value $\approx\sqrt{-8nU_0J\cos(ka)}\approx 27J$. Figure 6(b) plots a case with a much smaller nonlinearity ($nU_0/J=1$ and $nU_2/J=0.04$). While $ka < \pi/2$ is still the condition for stability of all the modes, one sees that for higher values of k there exists only a band of low unstable modes in the lower-q region. This is due to the fact that the right-hand side (RHS) of (22) becomes less than unity and thus can be exceeded by the LHS for large q.

Just as we saw in the two-component case (see Fig. 4), these conditions are somewhat reversed for attractive interactions $U_0<0$, as then some excitations of $\omega_{1+}(q)$ are unstable whenever $ka < \pi/2$ and all the q modes are unstable when $0 < \cos(ka) < -nU_0/(2J)$. The dependence on the interaction coefficient U_0 is shown in Fig. 7. In these plots, we kept $U_2n/J=2$ constant. For $ka=0.2\pi$ [Fig. 7(a)] unstable modes occur for negative U_0, while for $ka=0.7\pi$ [Fig. 7(b)], this instability occurs for repulsive interactions $U_0>0$. Also, as in the two-component case, there is an additional, weaker instability in the attractive case $U_0<0$ with $ka > \pi/2$. This instability is driven by $\omega_{2+}(q)$ and has the same condition for instability (22) with U_0 replaced by U_2. The magnitude generally reaches $\approx\sqrt{8nU_2J}$ for $nU_2\gg J$. In the case plotted in Fig. 7(b), it has a maximum magnitude $\approx 2J$.

The equivalence of the mode energy dependence on U_2 and U_0 in Eq. (19) implies that whenever U_0 and U_2 are of opposite sign and much larger than J, at least one of the eigenvalues will be imaginary at any k. In the previous paragraph we discussed how this resulted in an instability for attractive condensates $U_0<0$ with polar spin-dependent scat-
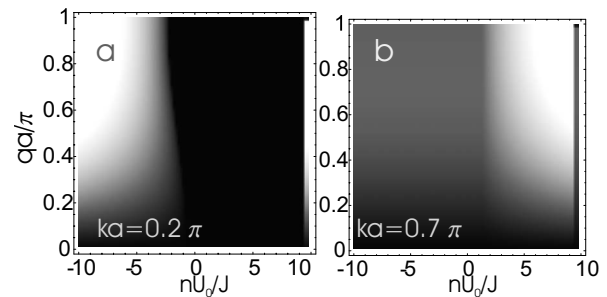
tering lengths $U_2>0$. Another implication of this is that polarlike condensate solutions (18) with $U_0>0$ are unstable for ferromagnetic spin-dependent scattering lengths $U_2<0$. Only when both are positive or both are negative is there a region of k with dynamical stability.

2. Energetic stability

Turning now to the energetic instabilities, we also obtain analytic results for the eigenvalues of $\mathcal{M}$ and look for negative eigenvalues. We find

$$\epsilon_{1\pm}(q) = \epsilon_q\cos(ka) + nU_0 \pm \sqrt{C_{q,k}^2 + n^2U_0^2},$$

$$\epsilon_{2\pm}(q) = \epsilon_q\cos(ka) + nU_2 \pm \sqrt{C_{q,k}^2 + n^2U_2^2}. \tag{23}$$

For $U_2 < U_0$, ϵ_{2-} drives the instability. Figure 8 plots the regions of energetic instability. There exist unstable modes for $\cos(ka)/\sin^2(ka) < 2J/nU_2$. For small velocities, $ka \ll 1$, this condition is approximately equal to $\hbar k/m^* > \sqrt{nU_2/m^*}$, where $m^* = \hbar^2/(2Ja^2)$ is the effective mass of a noninteracting BEC. This energetic instability threshold demonstrates the Landau criterion that the velocity becomes larger than the speed of sound (of spin waves) $a\sqrt{2JnU_2}/\hbar = \sqrt{nU_2/m^*}$. For $U_2 > U_0$ the instability driven by ϵ_{1-} and the condition is the same, but replacing $U_2 \to U_0$. When U_0 becomes negative, there is an additional instability, as shown in Fig. 8(b).

FIG. 7. Imaginary part of the eigenvalues versus nU_0, for $nU_2=2J$ for the condensate velocities indicated. Gray scale goes from 0 to $5J$.
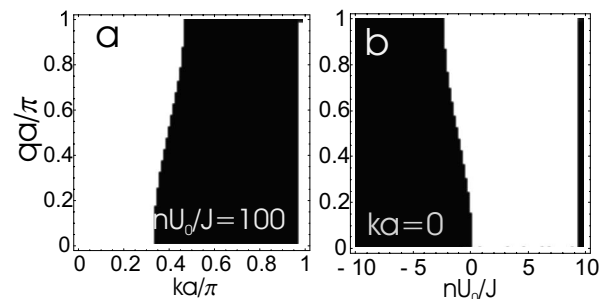

FIG. 8. (a) Energetic stability (white) and instability (black) regions for $nU_0=100J$, $nU_2=4J$. (b) Dependence of the energetic stability of interaction coefficient nU_0, keeping $nU_2=2J$. The behavior remains qualitatively the same for nonzero $ka < \pi/2$, but with the instability region extending into the $U_0>0$ region.
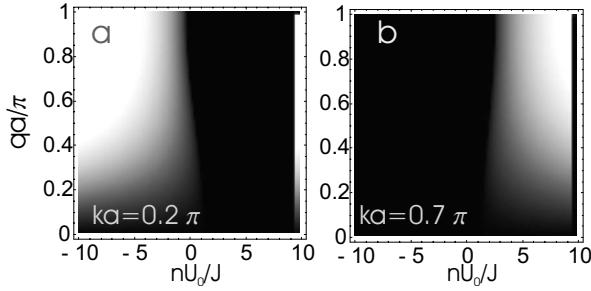
FIG. 9. Imaginary part of the eigenvalues (19) versus nU_0, holding $nU_2 = -2J$, for the two condensate velocities indicated. Gray scale goes from 0 to $5J$.

C. Stability in the ferromagnetic case

1. Dynamical stability

In the ferromagnetic case (which is energetically favored for $U_2 < 0$), we consider uniform spin profiles for which the magnitude of the spin is maximized, $|\langle \mathbf{F} \rangle| = 1$, which minimizes the mean-field energy (15). We again assume no magnetic Zeeman shifts $\delta_+ = \delta_- = 0$. As in analogous states for superfluid liquid helium-3 [53], the rotations of the spinor axes can be used to couple physically distinguishable ground states. Here all the degenerate states are related by spatial rotations of the atomic spin axes and we may parametrize the spin wave function as

$$\begin{pmatrix} \zeta_+ \\ \zeta_0 \\ \zeta_- \end{pmatrix} = e^{i\phi} \begin{pmatrix} e^{-i\alpha} \cos^2(\beta/2) \\ \sin(\beta)/\sqrt{2} \\ e^{i\alpha} \sin^2(\beta/2) \end{pmatrix}, \quad (24)$$

where α, β, ϕ are the Euler angles. The solution (17) with Eq. (24) has a chemical potential $\mu = -2J \cos(ka) + (U_0 + U_2)n$ for any chosen ground state in Eq. (24). The simplest form of the Bogoliubov–de Gennes matrix $\sigma\mathcal{M}$ may be obtained by choosing $\beta = \alpha = \phi = 0$ and substituting Eq. (24) into Eq. (A2) in Appendix A.

The mode energies are found to be

$$\omega_{1\pm}(q) = C_{q,k} \pm \epsilon_q \cos(ka),$$

$$\omega_{2\pm}(q) = C_{q,k} \pm \epsilon_q \cos(ka) \mp 2nU_2,$$

$$\omega_{3\pm}(q) = C_{q,k} \pm \sqrt{\epsilon_q \cos(ka)[\epsilon_q \cos(ka) + 2n(U_0 + U_2)]}.$$
$$(25)$$

The dynamical instabilities are driven entirely by ω_{3+} and the only difference with the polar case Eq. (19) is the replacement U_0 and U_2 individually by the sum $U_0 + U_2$. This dependence can be understood from the fact that with $|\langle \mathbf{F} \rangle| = 1$ the total nonlinearity is proportional to $U_0 + U_2$ and so this quantity determines the attractive or repulsive character of the condensate. Thus for $U_0 > 0$ and $|U_2| \ll |U_0|$, the instability diagrams qualitatively similar to Fig. 6.

Differences between the ferromagnetic and polar cases become clear when one examines the instability dependence on U_0. This is shown for the ferromagnetic case in Fig. 9,
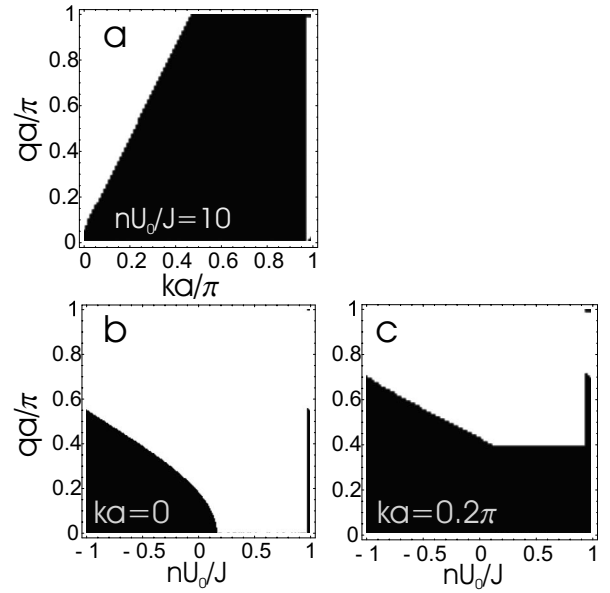

FIG. 10. (a) Energetic stability regions for the ferromagnetic case with ^{87}Rb parameters $U_0 = 100J$, $U_2 = -0.36J$. (b), (c) Energetic stability versus the interaction coefficient U_0, keeping $U_2 = -2J$.

where we keep $nU_2 = -2J$ constant, and should be contrasted with the polar case, Fig. 7. For $ka < \pi/2$ (the figure shows $ka = 0.2\pi$), an instability occurs for $U_0 < -U_2$ and increases with greater $|U_0|$ while for $ka > \pi/2$ (the figure shows $ka = 0.7\pi$), the instability occurs for $U_0 > -U_2$. An important difference from the polar case is that, for $ka > \pi/2$, there is no instability for $U_0 < 0$. In addition, the instability border occurs at $U_0 = -U_2$ rather than at $U_0 = 0$. Finally, from Eq. (25), we note that a ferromagnetic BEC solution (24) with $U_0 > 0$ and a *polar* spin-dependent scattering length $U_2 > 0$ can be dynamically stable, in contrast to a polar solution with ferromagnetic scattering length, as discussed above.

2. Energetic stability

The energy eigenvalues in the ferromagnetic case are

$$\epsilon_{1\pm}(q) = \epsilon_q \cos(ka) \pm C_{q,k},$$

$$\epsilon_{2\pm}(q) = \epsilon_q \cos(ka) - 2nU_2 \pm C_{q,k},$$

$$\epsilon_{3\pm}(q) = \epsilon_q \cos(ka) + n(U_0 + U_2) \pm \sqrt{C_{q,k}^2 + n^2(U_0 + U_2)^2}.$$
$$(26)$$

Unlike the polar case, there is one energy eigenvalue ϵ_{1-} corresponding to a pure (Doppler-shifted) kinetic energy. This gives rise to energetic instabilities for $\sin^2(qa/2)/\sin(qa) < \tan(ka)$, as plotted in Fig. 10(a). Though no dynamic instability exists except for much higher k, ferromagnetic spinor BECs are subject to this energetic instability in the presence of thermal excitation for any nonzero k. We note that for $ka > 0.5\pi$ all q modes are unstable.

Finally, for attractive condensates ($U_0 + U_2 < 0$) there are additional regions of energetic instability from ϵ_{3-}. Figures 10(b) and 10(c) shows the dependence versus U_0. For $k = 0$

there are unstable modes for all attractive condensate scattering length cases. A moving condensate [$ka = 0.2\pi$ is shown in Fig. 10(c)] increases the region of unstable q modes for attractive condensates. The band of energetic instability at low q for $U_0 > 0$ in Fig. 10(c) is simply the Doppler-induced energetic instability discussed above.

D. Effects of Zeeman splitting

When Zeeman splittings due an external magnetic field [$\delta_\pm$ in Eq. (16)] are nonzero, the symmetry of the polar and ferromagnetic solutions, Eqs. (18) and (24), breaks down and we find a new set of steady-state solutions. Here we examine these solutions and again calculate the dynamic stability of these various solutions, particularly noting how the stability varies with the *linear* and *quadratic* Zeeman shifts, which we denote, respectively, as $\tilde{\delta} = (\delta_+ - \delta_-)/2$ and $\bar{\delta} = (\delta_+ + \delta_-)/2$. The linear Zeeman shifts are $\tilde{\delta} = 2g_F\mu_B B = 2[(2\pi)1.4 \text{ MHz/G}]B$, where g_F is the Landé factor, and is $-1/2$ for the ground-state $F = 1$ manifold of ^{87}Rb and ^{23}Na. For Zeeman shifts substantially smaller than the hyperfine splitting, which is our interest here, the quadratic shifts $\bar{\delta}$ are typically smaller than the linear shifts and can be extracted from the Breit-Rabi formula [54]. For alkali-metal atoms, the quadratic shift is positive, but it can generally be of either sign. The level shifts in a spin-1 BEC may also be engineered in other ways, e.g., by using off-resonant microwave fields that generate electromagnetically induced level splittings [55], allowing essentially arbitrary experimentally prepared level shifts for $\tilde{\delta}$ and $\bar{\delta}$. Note that the linear Zeeman shift does not affect the energy conservation of a spin-changing collision $|m_F = 0, m_F = 0\rangle \leftrightarrow |m_F = +1, m_F = -1\rangle$, while the quadratic Zeeman shift does, and thus plays an important role in the stability properties.

One of the steady-state solutions in the presence of the Zeeman splitting has the chemical potential $\mu = \mu_0 = -2J\cos(ka) + nU_0$ and reads

$$\vec{\zeta} = e^{i\varphi}\begin{pmatrix} 0 \\ 1 \\ 0 \end{pmatrix}. \quad (27)$$

This solution forms a subset of the polar solutions (18) in the absence of the magnetic splitting, with the **d** pointing along the z direction.

The stability is again analyzed by substituting the steady-state solution [Eq. (27)] into Eq. (A2). By calculating the eigenvalues of $\sigma\mathcal{M}$ we obtain analytic expressions for the normal mode energies, as in Eq. (19). Here $\omega_{1\pm}(q)$ remains unchanged in the presence of the Zeeman splitting and

$$\omega_{2\pm}(q) = C_{q,k} \pm \tilde{\delta} \pm P_{q,k},$$

$$\omega_{3\pm}(q) = C_{q,k} \mp \tilde{\delta} \pm P_{q,k},$$

$$P_{q,k} = \sqrt{[\epsilon_q \cos(ka) + \bar{\delta}][\epsilon_q \cos(ka) + 2nU_2 + \bar{\delta}]}. \quad (28)$$

The linear splitting lifts the degeneracy between $\omega_{2\pm}(q)$ and $\omega_{3\pm}(q)$ in Eq. (19) and the quadratic splitting introduces an energy gap $\bar{\delta}$ in the single-particle phonon mode spectrum $\epsilon_q \cos(ka)$ in $\omega_{2\pm}(q)$ and $\omega_{3\pm}(q)$.

The dynamical stability will then be governed by the sign of the square root argument of $P_{q,k}$ and is seen to be unaffected by the linear Zeeman shift. The condition for the existence of unstable modes is $-\epsilon_q \cos(ka) - 2nU_2 < \bar{\delta} < -\epsilon_q \cos(ka)$ for $U_2 > 0$, and $-\epsilon_q \cos(ka) < \bar{\delta} < -\epsilon_q \cos(ka) - 2nU_2$ for $U_2 < 0$. If $U_2 > 0$ and $ka < \pi/2$, Eq. (28) predicts dynamical stability for positive quadratic shift $\bar{\delta} > 0$, and instability at some q for $\bar{\delta} < 0$. As in previous cases, we find much larger instabilities when $ka > \pi/2$ (for $U_0 > 0$) from $\omega_{1\pm}$.

Similarly, we obtain the eigenvalues of $\mathcal{M}$ as in Eq. (23). Here $\epsilon_{1\pm}(q)$ is unchanged and

$$\epsilon_{2\pm}(q) = \epsilon_q \cos(ka) + nU_2 + \bar{\delta} \pm \sqrt{(C_{q,k} + \tilde{\delta})^2 + n^2 U_2^2},$$

$$\epsilon_{3\pm}(q) = \epsilon_q \cos(ka) + nU_2 + \bar{\delta} \pm \sqrt{(C_{q,k} - \tilde{\delta})^2 + n^2 U_2^2}. \quad (29)$$

We find another steady-state solution to the DNLSEs (16) with the chemical potential $\mu = \mu_0 + \bar{\delta}$ that reads

$$\vec{\zeta} = \frac{e^{i\varphi}}{\sqrt{2}}\begin{pmatrix} e^{-i\gamma}\sqrt{1 - \tilde{\delta}/nU_2} \\ 0 \\ e^{i\gamma}\sqrt{1 + \tilde{\delta}/nU_2} \end{pmatrix}. \quad (30)$$

This solution only exists for sufficiently small linear Zeeman shifts $|\tilde{\delta}| < |nU_2|$. For $\tilde{\delta} = 0$, Eq. (30) coincides with the subset of solutions to Eq. (18). Although for small $\tilde{\delta} \neq 0$ the solution (30) is still close to the polar state of Eq. (18), the spin expectation value is no longer zero, $\langle \mathbf{F} \rangle = -\tilde{\delta}/(nU_2)\hat{\mathbf{z}}$, with **d** restricted on the xy plane and the induced $\langle \mathbf{F} \rangle$ pointing along the z axis [56]. At the boundary of the validity of Eq. (18), $\tilde{\delta} = \pm nU_2$, we obtain $\langle \mathbf{F} \rangle = \mp \hat{\mathbf{z}}$, as in a ferromagnetic state, so that Eq. (30) in fact interpolates between the polar and the ferromagnetic solutions. Moreover, we again find analytic solutions for the normal mode energies:

$$\omega_{1\pm}(q) = C_{q,k} \pm \sqrt{\epsilon_q \cos(ka)[\epsilon_q \cos(ka) + 2nU_2 - 2\bar{\delta}] + \tilde{\delta}^2 + \bar{\delta}^2 - 2nU_2\bar{\delta}},$$

$$\omega_{2\pm}(q) = C_{q,k} \pm \sqrt{\epsilon_q \cos(ka)[\epsilon_q \cos(ka) + n(U_0 + U_2)] + L_{q,k}},$$

$$\omega_{3\pm}(q) = C_{q,k} \pm \sqrt{\epsilon_q \cos(ka)[\epsilon_q \cos(ka) + n(U_0 + U_2)] - L_{q,k}},$$

$$L_{q,k} = \sqrt{\epsilon_q^2 \cos^2(ka)[n^2(U_0 - U_2)^2 + 4\widetilde{\delta}^2 U_0/U_2]}. \tag{31}$$

For $U_0, U_2 > 0$ and $ka < \pi/2$, whenever the solution (30) exists (i.e., when $|nU_2| \geqslant |\widetilde{\delta}|$), the dynamical instabilities are solely driven by $\omega_{1\pm}(q)$. Moreover, under these conditions the mode $\omega_{1\pm}(q)$ is dynamically stable when Eq. (30) is energetically favorable to Eq. (27) (i.e., when $\overline{\delta} < 0$). In Fig. 11 we show some stability diagrams for the parameters of ^{23}Na. The instability dependence on the quadratic Zeeman shift for a particular linear Zeeman shift is shown in Fig. 11(a). This diagram may be understood by noting that the mode $\omega_{1\pm}(q)$ exhibits a nonvanishing imaginary part, if

$$c_- < \overline{\delta} < c_+,$$

$$c_\pm \equiv \epsilon_q \cos(ka) + nU_2 \pm \sqrt{n^2 U_2^2 - \widetilde{\delta}^2}. \tag{32}$$

This forms an instability stripe with a width $2(n^2 U_2^2 - \widetilde{\delta}^2)^{1/2}$ in Fig. 11(a) and for larger values of $\overline{\delta}$ the system stabilizes again. We observe the stripe position shift in $\overline{\delta}$ by $4J$ from the $qa = 0$ to $qa = \pi$. We also calculated the energetic stability of Eq. (30) and found that in Fig. 11(a) the region to the left of the stripe is energetically stable, while the entire region to the right of the stripe (i.e., large $\overline{\delta}$) is energetically unstable.

While not obvious in Fig. 11(a) there is a small region of stability for positive $\overline{\delta}$. This is seen more easily by plotting the instability versus the linear Zeeman shift. In Figs. 11(b)–11(d) we plot this for the entire range of validity of Eq. (30) ($|\widetilde{\delta}| \leqslant |nU_2|$) for various $\overline{\delta}$. For small quadratic Zeeman shift, there exists a range of linear Zeeman shifts which stabilize the system, as it approaches the ferromagnetic state. For larger quadratic shifts this range shrinks, until eventually the system is unstable at all possible $\widetilde{\delta}$, as in Fig. 11(b).

The effect of larger k is generally simply to stretch the region of instability to larger ranges of q for each case, as the effect of the ϵ_q shift in Eq. (32) vanishes. For $ka > 0.5\pi$ (with $U_0 > 0$) the usual, and much larger, instability for large k, seen in previous cases, dominates the stability diagram. Such a case is plotted in Fig. 11(d).

In the absence of the Zeeman splitting the polar state (18) is always dynamically unstable for $U_2 < 0$. For the state (30), even close to the polar state, this is no longer the case. For $U_0 > 0$ and $U_2 < 0$, Eq. (32) represents the entire unstable region, provided that $4\widetilde{\delta}^2 |U_0/U_2| \leqslant n^2(U_0 - U_2)^2$ and $|U_0| > |U_2|$.

In the presence of the Zeeman splitting the ferromagnetic state (24) is modified to

$$\vec{\zeta} = e^{i\phi}\begin{pmatrix} 1 \\ 0 \\ 0 \end{pmatrix}, \tag{33}$$

with the chemical potential $\mu = \mu_0 + nU_2 + \delta_+$, or to an analogous ferromagnetic state with (ζ_+, δ_+) interchanged with

(ζ_-, δ_-). Although Eq. (33) is a steady-state solution to the DNLSEs (16) for any values of $\widetilde{\delta}$, we also find that the solution (30) has the limit Eq. (33) at the boundary of the validity region $\widetilde{\delta} = -nU_2$. At the other limit of the validity of Eq. (30) (at $\widetilde{\delta} = nU_2$) we recover the other ferromagnetic state, defined by (ζ_-, δ_-). Moreover, the solution (33) is energetically favorable to Eq. (27) when $nU_2/2 + \delta_+ < 0$ and to Eq. (30) when $nU_2/2 + \widetilde{\delta} < 0$.

We find that the normal mode energies and the eigenvalues of $\mathcal{M}$ corresponding to Eq. (33) are obtained from the non-Zeeman-shifted mode frequencies, Eqs. (25) and (26), by shifting the single-particle excitation energies: $\epsilon_q \cos(ka) \to \epsilon_q \cos(ka) - \delta_+$ in $\omega_{1\pm}(q)$ and $\epsilon_{1\pm}(q)$; and $\epsilon_q \cos(ka) \to \epsilon_q \cos(ka) - 2\widetilde{\delta}$ in $\omega_{2\pm}(q)$ and $\epsilon_{2\pm}(q)$. The energies $\omega_{3\pm}(q)$ and $\epsilon_{3\pm}(q)$ are unchanged. Because it is $\omega_{3\pm}$ that drives the dynamical instability, the stability diagram is unchanged from that of Eq. (25).

We find an additional ferromagneticlike steady-state solution to the DNLSEs (16) with $\mu = \mu_0 + nU_2 + (\overline{\delta}^2 - \widetilde{\delta}^2)/2\overline{\delta}$, which reads

$$\zeta_\pm = e^{i\gamma_\pm}\delta_\mp \sqrt{\frac{2nU_2\overline{\delta} + \overline{\delta}^2 - \widetilde{\delta}^2}{8nU_2\overline{\delta}^3}},$$

$$\zeta_0 = e^{i(\gamma_+ + \gamma_-)/2}\sqrt{1 - |\zeta_+|^2 - |\zeta_-|^2}. \tag{34}$$

This solution exists only if the expressions inside the square roots of Eq. (34) are positive, i.e.,

$$0 \leqslant \frac{2nU_2\overline{\delta} + \overline{\delta}^2 - \widetilde{\delta}^2}{8nU_2\overline{\delta}^3} \leqslant \frac{1}{2(\widetilde{\delta}^2 + \overline{\delta}^2)}. \tag{35}$$

This condition gives rise to a ranges of validity for U_2 in terms of two parameters $\beta_- = (\widetilde{\delta}^2 - \overline{\delta}^2)/2\overline{\delta}$ and $\beta_+ = (\widetilde{\delta}^2 + \overline{\delta}^2)/2\overline{\delta}$. In the most common case that the linear Zeeman shift is larger in magnitude ($|\widetilde{\delta}| > |\overline{\delta}|$) these inequalities give a finite range: $\beta_- < nU_2 < \beta_+$ for $\overline{\delta} > 0$ and $\beta_+ < nU_2 < \beta_-$ for $\overline{\delta} < 0$.

If $|\widetilde{\delta}| < |\overline{\delta}|$, the inequalities change direction, giving instead an intermediate range of U_2 where (34) is *not* valid. In particular, the requirement for validity for $\overline{\delta} > 0$ is $nU_2 < \beta_-$ or $nU_2 > \beta_+$, while for $\overline{\delta} < 0$ it is $nU_2 < \beta_+$ or $nU_2 > \beta_-$.

At the lower limit of Eq. (35) ($nU_2 = \beta_-$) the solution (34) coincides with the polar solution (27) with $\langle \mathbf{F} \rangle = \mathbf{0}$, while at the upper limit ($nU_2 = \beta_+$) it equals Eq. (30). In general, the spin for the solution (34) is nonvanishing
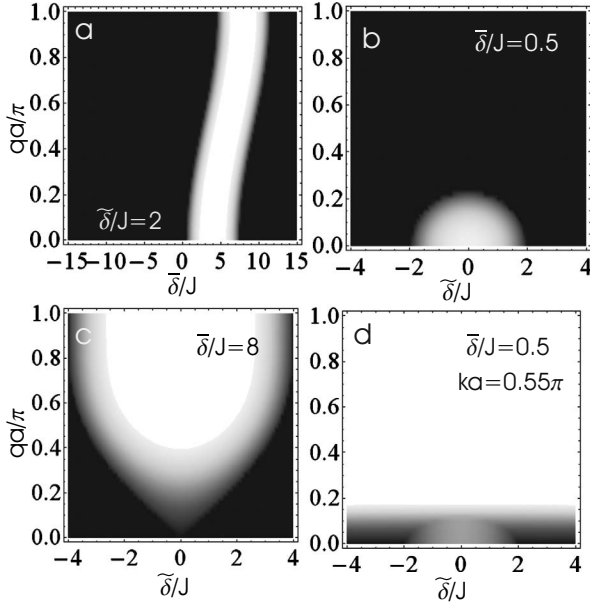
FIG. 11. Largest imaginary parts of the normal mode energies for the polarlike solution Eq. (30). In all plots, $U_0=100J$ and $U_2=0.04U_0$ (corresponding to ^{23}Na). Plots are on a gray scale of 0 to $3J$. (a) Dynamic instability versus $\bar{\delta}$ for linear Zeeman shift $\tilde{\delta}=2J$ and $k=0$. (b), (c) Versus linear shift $\tilde{\delta}$ for quadratic Zeeman shifts $\bar{\delta}=0.5J$ and $8J$, with $k=0$. (d) Versus $\tilde{\delta}$ with $ka=0.55\pi$.

$$|\langle \mathbf{F} \rangle|^2 = \frac{2\bar{\delta}^2(\tilde{\delta}^2 + 2n^2U_2^2) - \bar{\delta}^4 - \tilde{\delta}^4}{4\bar{\delta}^2 n^2 U_2^2}. \qquad (36)$$

This condensate solution (34) is energetically favorable to (33) for *positive* quadratic shifts $\bar{\delta}>0$, the opposite relationship of solution (30) to (27).

We computed the dynamical and energetic stability of this solution. Figures 12(a)–12(c) show the dynamical instability strengths as a function linear Zeeman shift for several quadratic shifts and ^{87}Rb scattering length ($U_2=-0.0036U_0$). The hatched areas and all $|\tilde{\delta}|$ larger than the range of these plots are regions where the condensate solution (34) is not valid. For $\bar{\delta}>0$ [Fig. 12(a)] we see that the valid regions where the solution exists are dynamically stable. For $\bar{\delta}<0$ [Figs. 12(b) and 12(c)] there are always some unstable modes q. However, note the interesting behavior that for large $|\tilde{\delta}|$ there exist only small bands of unstable q and weak instability (note the range of the plots in the caption). The system is *energetically* unstable for q in the regions overlapping and below the small dynamical instability bands.

In Fig. 12(d) we plot the instability strength versus U_2 over its range of validity, which in this case is $1.5J<nU_2<2.5J$. Here we see a weak band of instability for low q in the range of U_2 where the solution exists.

IV. EXPERIMENTAL CONSIDERATIONS

In the experimental realizations of optical lattice systems, ultracold atoms have been trapped in a combined optical
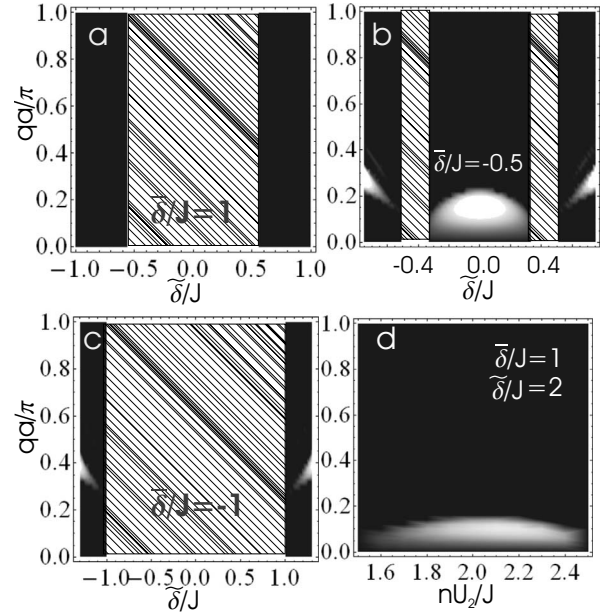

FIG. 12. Largest imaginary parts of the normal mode energies for the solution Eq. (34). In all plots, $nU_0=100J$. Hatched areas represent regions where the condensate solution is not valid. (a)–(c) Dynamic instability versus linear Zeeman shift and q for $U_2=-0.0036U_0$ (corresponding to ^{87}Rb). Gray scale runs from (a) 0 to $0.3J$, (b) 0 to $0.3J$, and (c) 0 to $0.2J$. In (a) we emphasize that there is a range of $\tilde{\delta}$, on each side of the instability region, stable for all q. (d) Dynamic instability versus spin-dependent scattering length U_2 for $\tilde{\delta}=2J$ and $\bar{\delta}=J$. Gray scale from 0 to $0.2J$.

lattice and a harmonic trap. The transport properties may then be studied by suddenly displacing the harmonic trap, e.g., by using a magnetic field gradient. This excites dipolar oscillations of atoms along the lattice direction with the maximum velocity proportional to the harmonic trap displacement [2,9]. The other alternative is to use a moving-standing wave, so that the atoms are trapped close to the harmonic trap minimum and experience a moving optical lattice potential [7,8]. The advantage of the latter technique is that the velocity of the atoms with respect to the lattice is constant. In such transport experiments the dynamical instabilities may typically be observed on much shorter time scales than the energetic ones and the rate of the energetic instability to have an observable effect can be controlled by increasing the size of the thermal atom cloud [8].

A two-component ultracold ^{87}Rb vapor has also been trapped in a spin-dependent lattice using two counterpropagating laser beams with linear polarizations [31]. The two species experience different σ_+ and σ_- polarized optical lattices where the separation between the lattice potentials can be controlled by changing the angle between the linear polarization vectors.

The techniques developed for investigating dynamical and energetic instabilities in a single component case could be adapted to our proposed two-component BEC studies. A spin-dependent lattice potential may be used to control the value of the intraspecies interaction strength U_{12} by modifying the spatial overlap integral between the lattice site wave

functions of the two species. Moreover, the various intra- and interspecies scattering lengths and the two-species Feshbach resonances [57] in two-component BEC systems make them a very rich area for experimental exploration. In addition to the two-component ^{87}Rb vapor [31], two-component BECs have been experimentally realized in optical lattices using a ^{41}K-^{87}Rb mixture [32].

Different superfluid velocities for the two species can be realized in such a system by moving the two lattice potentials at different speeds. The disadvantage of this scheme is that it would make the intraspecies interaction strength U_{12} time dependent. Displacing the harmonic trapping potentials of the two BECs different distances, in such a way that at the end the traps are perfectly overlapping, could be used to realize two BECs undergoing dipolar oscillations in phase with different amplitudes. Perhaps the easiest method to measure the reversed phase separation instability in a two-species BEC, as discussed in Sec. II B 3 and Appendix B, is to move the lattice potentials of the both species at the same speed and to use light-stimulated coherent Bragg diffraction [58] to change the velocity of one of the BECs. For sufficiently small velocities of the Bragg-diffracted BEC, the atomic clouds of the two BECs overlap long enough for the dynamical instabilities to have an observable effect.

Atomic ^{87}Rb spin-1 gases have also been loaded to optical lattices [44]. In such a system the linear and quadratic Zeeman shifts could be modified, e.g., by using off-resonant microwave field-induced level shifts [55]. This would allow the studies of the stability properties of different steady-state solutions presented here.

V. CONCLUSIONS

We studied the transport properties of two-component and spinor atomic BECs in optical lattices using the discrete nonlinear Schrödinger equations, obtained in the tight-binding approximation to the lattice system. The classical GP theory is valid in optical lattices at low temperatures if the effective 1D nonlinearity is not too large, the atom number not too small, or the lattice potential not too deep [59]. In particular, we studied both the dynamical and energetic stability of homogenous Bloch wave solutions to the DNLSEs for the condensates by analyzing the linearized perturbations around the carrier wave. In the case of the dynamical instabilities this involved finding the eigenvalues (normal mode energies) of the corresponding Bogoliubov–de Gennes equations [the matrix $\sigma\mathcal{M}$ in Eq. (5)] and in the case of energetic instabilities finding the eigenvalues of the second-order perturbations in the energy functional (the matrix $\mathcal{M}$). Our steady-state Bloch wave ansatz allowed for magnetic Zeeman level shifts and even for two different velocities of the condensates in the two-component case. Our study discusses a large number of cases and points out how the spin degree of freedom can affect the stability properties.

In the two-component case we analyzed and fully characterized the dynamical and energetic instabilities for the general case of the two BECs exhibiting arbitrary hopping amplitudes, interaction strengths, superfluid velocities, and spatial overlap. Simple analytic expressions for the normal mode energies [Eq. (6)] and the dynamical stability criteria were obtained in the important case of the two BECs having the same atom current (even when the velocities may differ).

For the case that $\cos(k_1 a)$ and $\cos(k_2 a)$ exhibit equal sign for the two BEC carrier wavenumbers k_1, k_2 (see Sec. II B 2), we found that the instability diagram contains contributions from (1) the high-velocity instability, determined by Eq. (12) (which is analogous to that of a single-component BEC in a lattice), and (2) a weaker phase separation instability [Eq. (13)], which occurs when $U_{12}^2 > U_{11}U_{22}$. However, as shown in Appendix B and in Sec. II B 3, an interesting case arises when one allows different condensate velocities of the two components, so that $\cos(k_1 a)$ and $\cos(k_2 a)$ exhibit different signs (the effective masses of the two components exhibit different signs). First, the high-velocity instability conditions (which depends on the velocities, hopping amplitudes, atom numbers, and interaction strengths of the two BECs) indicate that the presence of the other condensate component can stabilize the superfluid flow of an otherwise unstable condensate (that exceeds the critical velocity of a single-component BEC). Second, the phase separation stability criteria can be reversed for particular sets of parameters and the entire dynamically *stable* regime exists for $U_{12}^2 > U_{11}U_{22}$; see Appendix B and Figs. 3(c) and 3(d).

For the spin-1 BEC case, we also obtained analytic expressions for the dynamical and energetic instabilities in several cases of interest. In the absence of the Zeeman level shifts the normal mode energies in the polar and ferromagnetic ground state manifolds are simplified and the two cases differ when $U_0 < 0$ and for relatively large spin-dependent interactions $|U_2| \sim |U_0|$. In particular, the polar case tends to exhibit more regions of instability as U_0 and U_2 separately contribute [see Eq. (19)], while in the ferromagnetic case, it is the sum $U_0 + U_2$ which is important; see Eq. (25). This allows for dynamical stability of ferromagnetic solutions for $U_0 < 0$, and even for polar spin-dependent scattering lengths ($U_2 > 0$). Also, we found that, unlike the polar case, the ferromagnetic solution will have some *energetic* instability for any finite BEC velocity due to the existence of a pure kinetic energy eigenvalue $\epsilon_{1\pm}$ [Eq. (26)].

In the presence of the linear and quadratic Zeeman level shifts we find a new set of steady-state Bloch wave solutions, describing the superfluid flow in spin-1 BECs. While the polarlike solution (27) and the ferromagneticlike solution (33) form subsets of the corresponding solutions in the absence of the Zeeman splitting, this is not the case for the steady-state solutions (30) and (34). The solution (30) exhibits a nonvanishing spin vector $\langle \mathbf{F} \rangle$ pointing along the magnetic field and interpolates between the polar and the ferromagnetic solutions. The solution (34) only exists in the presence of sufficiently large Zeeman shifts and in this sense represents an entirely novel state.

We analyzed the stability conditions for all spin-1 Bloch wave states. For condensate solutions unique to the presence of Zeeman shift, Eqs. (30) and (34), the stability diagrams were presented in Figs. 11 and 12, respectively. For the parameters of ^{23}Na at low velocities we found the solution Eq. (30) to be dynamically stable for negative quadratic shifts. Even for positive quadratic shift, a sufficiently large linear

shift can stabilize it. Moreover, the solution (30) can be stable for ferromagnetic scattering coefficients ($U_2 < 0$), even close to the polar state. For the parameters of ^{87}Rb the solution Eq. (34) can be energetically and dynamically stable for positive quadratic Zeeman shifts and sufficiently large linear Zeeman shifts.

The phenomena discussed in this paper should be applicable to current and future experiments with multiple-component BECs in optical lattices, and we discussed some of the important considerations for the experimental realization. We concentrated on the stability studies of moving Bloch wave solutions in the lattice. An interesting theoretical extension of this work is to consider inhomogenous condensate solutions, such as solitonlike structures in spinor BECs [47]. One could also investigate the effect of spin-dependent lattice potentials with spatially inhomogeneous profiles for the hopping amplitude, for instance dimerization, along the lattice [60].

ACKNOWLEDGMENTS

APPENDIX A: BOGOLIUBOV–DE GENNES MATRICES

In the two-component case, the Bogoliubov–de Gennes equation, upon substitution of the the ansatz (4) into (2), we get (5) with

$$
\mathcal{M} = \begin{pmatrix}
K_{1+} + \bar{U}_1 & -\bar{U}_1 & \bar{U}_{12} & -\bar{U}_{12} \\
-\bar{U}_1 & K_{1-} + \bar{U}_1 & -\bar{U}_{12} & \bar{U}_{12} \\
\bar{U}_{12} & -\bar{U}_{12} & K_{2+} + \bar{U}_2 & -\bar{U}_2 \\
-\bar{U}_{12} & \bar{U}_{12} & -\bar{U}_2 & K_{2-} + \bar{U}_2
\end{pmatrix}
\tag{A1}
$$

where

$$
K_{j\pm} = (4J_j/\hbar)\sin^2(qa/2)\cos(k_ja) \pm (2J_j/\hbar)\sin(qa)\sin(k_ja),
$$

$\bar{U}_j = U_{jj}n_j/\hbar$, and $\bar{U}_{12} = U_{12}\sqrt{n_1 n_2}/\hbar$.

In the general spinor case, we obtain the $\mathcal{M}$ for the spinor wave function and the Bogoliubov expansion (4), and substitute into the DNLSEs (16):

$$
\mathcal{M} = \begin{pmatrix}
M_-^{(+)} & w_{++} & f_{0+}^{0-} & w_{0+} & r_{-+} & g_{-+}^0 \\
(w_{++})^* & M_+^{(+)} & (w_{0+})^* & (f_{0+}^{0-})^* & (g_{-+}^0)^* & (r_{-+})^* \\
(f_{0+}^{0-})^* & w_{0+} & M_-^{(0)} & h_0^{-+} & (f_{0-}^{0+})^* & w_{0-} \\
(w_{0+})^* & f_{0+}^{0-} & (h_0^{-+})^* & M_+^{(0)} & (w_{0-})^* & f_{0-}^{0+} \\
(r_{-+})^* & g_{-+}^0 & f_{0-}^{0+} & w_{0-} & M_-^{(-)} & w_{--} \\
(g_{-+}^0)^* & r_{-+} & (w_{0-})^* & (f_{0-}^{0+})^* & (w_{--})^* & M_+^{(-)}
\end{pmatrix},
\tag{A2}
$$

$$
M_\pm^{(+)} = K_\pm + \bar{U}(1 + |\zeta_+|^2) + \tilde{U}(2|\zeta_+|^2 + |\zeta_0|^2 - |\zeta_-|^2) + \delta_+,
\tag{A3}
$$

$$
M_\pm^{(0)} = K_\pm + \bar{U}(1 + |\zeta_0|^2) + \tilde{U}(|\zeta_+|^2 + |\zeta_-|^2),
\tag{A4}
$$

$$
M_\pm^{(-)} = K_\pm + \bar{U}(1 + |\zeta_-|^2) + \tilde{U}(-|\zeta_+|^2 + |\zeta_0|^2 + 2|\zeta_-|^2) + \delta_-,
\tag{A5}
$$

$$
f_{kl}^{mn} = (\bar{U} + \tilde{U})\zeta_k^* \zeta_l + 2\tilde{U}\zeta_m\zeta_n^*,
\tag{A6}
$$

$$
g_{kl}^m = (\tilde{U} - \bar{U})\zeta_k\zeta_l - \tilde{U}\zeta_m^2,
\tag{A7}
$$

$$
h_k^{lm} = -\bar{U}\zeta_k^2 - 2\tilde{U}\zeta_l\zeta_m,
\tag{A8}
$$

$$
w_{kl} = -(\bar{U} + \tilde{U})\zeta_k\zeta_l,
\tag{A9}
$$

$$
r_{kl} = (\bar{U} - \tilde{U})\zeta_k^* \zeta_l.
\tag{A10}
$$

Here $\bar{U} = nU_0/\hbar$, $\tilde{U} = nU_2/\hbar$, and

$$
\begin{aligned}
K_\pm = &-2(J/\hbar)\cos(ka) \\
&+ (4J/\hbar)\sin^2(qa/2)\cos(ka) \pm (2J/\hbar)\sin(qa)\sin(ka) - \mu.
\end{aligned}
\tag{A11}
$$

APPENDIX B: DYNAMICAL STABILITY FOR $k_1a > \pi/2$, $k_2a < \pi/2$

In this section we analyze the dynamical stability of the two-component BEC system with equal atom currents $J_1 \sin(k_1a) = J_2 \sin(k_2a)$, when $\cos(k_1a)$ and $\cos(k_2a)$ exhibit different signs. Setting the atom currents to be equal allows us to obtain simple analytic expressions for the stability conditions. The different signs of $\cos(k_1a)$ and $\cos(k_2a)$ represent the situation where the velocities of the two BECs are located on the opposite sides of the deflection point in the ideal, single-particle BEC excitation spectrum (8) (the effective masses of the two components exhibit different signs). Without loss of generality we assume in the following that $\cos(k_1a) < 0$ and $\cos(k_2a) > 0$. The situation where when $\cos(k_1a)$ and $\cos(k_2a)$ have the equal sign is covered in Sec. II B.

The analytic result for the normal mode energies is given by Eq. (6). Similarly to the case when $\cos(k_1a)$ and $\cos(k_2a)$ have the same sign, the system is always dynamically unstable if $\omega_{1,q}^2 + \omega_{2,q}^2 < 0$ and we have the same condition as in Eq. (12):

$$
D_{11} + D_{22} < 0,
\tag{B1}
$$

where D_{ij} is defined in Eq. (11),

$$
D_{ij} = J_i \cos(k_ia)n_jU_{jj}.
\tag{B2}
$$

Since $k_1a > \pi/2$, $k_2a < \pi/2$, and $J_1, J_2 > 0$, the inequality may even be satisfied for some values for which $U_{11}, U_{22} > 0$. In this case only one of the BECs reaches the (single-component) critical velocity $ka = \pi/2$, destabilizing the entire two-component BEC system.

Next we assume $\omega_{1,q}^2 + \omega_{2,q}^2 \geq 0$ and find the additional unstable regions of the parameter space. When $\cos(k_1a)$ and

$\cos(k_2a)$ have different signs, the expression inside the inner square root in Eq. (6) may become negative, resulting in a dynamical instability. In particular, this happens at least for some values of q, if

$$U_{12}^2 > \xi_1, \tag{B3}$$

where

$$\xi_1 = -\frac{(D_{11} - D_{22})^2}{4n_1n_2J_1\cos(k_1a)J_2\cos(k_2a)}, \tag{B4}$$

where D_{ij} is defined in Eq. (11).

Also the expression inside the outer square root may become negative. If

$$n_1U_{11} < n_2U_{22} \min\left(\left| \frac{J_2\cos(k_2a)}{J_1\cos(k_1a)} \right|, \left| \frac{J_1\cos(k_1a)}{J_2\cos(k_2a)} \right| \right), \tag{B5}$$

this happens at least for some values of q, if $U_{11}U_{22} > U_{12}^2$. Combining this with Eq. (B3), we find that the system is *stable* for the values of U_{11} that satisfy Eq. (B5), if

$$U_{11}U_{22} < U_{12}^2 < \xi_1. \tag{B6}$$

Similarly, for the values of U_{11} satisfying

$$n_1U_{11} > n_2U_{22}\left| \frac{J_1\cos(k_1a)}{J_2\cos(k_2a)} \right| - 4J_1\cos(k_1a),$$

$$n_1U_{11} < n_2U_{22}\left| \frac{J_2\cos(k_2a)}{J_1\cos(k_1a)} \right|, \tag{B7}$$

we find that a dynamically *stable* system exists if

$$\xi_2 < U_{12}^2 < \xi_1, \tag{B8}$$

where

$$\begin{aligned}\xi_2 = {}& U_{11}U_{22} + 4J_1\cos(k_1a)J_2\cos(k_2a)/(n_1n_2) \\ &+ 2[J_1\cos(k_1a)U_{22}/n_1 + J_2\cos(k_2a)U_{11}/n_2]. \end{aligned} \tag{B9}$$

When U_{11} satisfies Eq. (B7), ξ_2 is always larger than $U_{11}U_{22}$ and for the dynamically stable region we have $U_{11}U_{22} < \xi_2 < U_{12}^2 < \xi_1$. If $\xi_2 > \xi_1$, no stable region exists.

Note that the *entire* stable region in both Eqs. (B6) and (B8) corresponds to the values of the nonlinearities satisfying $U_{11}U_{22} < U_{12}^2$ that is normally associated with the dynamically unstable phase separation condition.

The two-component system is therefore dynamically stable if $D_{11} + D_{22} > 0$ and U_{12} satisfies either Eq. (B6) or Eq. (B8), for U_{11} defined by Eq. (B5) or Eq. (B7), respectively. Interestingly, we find a regime where the other condensate component can stabilize the superfluid flow of an otherwise unstable condensate. The inequalities (B5) or (B7) can be satisfied for $U_{11}, U_{22} > 0$ when the component ψ_1 exceeds the critical velocity of the single-component BEC, with $k_1a > \pi/2$, so that $\omega_{1,q}^2 < 0$ in Eq. (7). The two-component BEC dynamics, nevertheless, is stable if U_{12} satisfies either Eq. (B6) or Eq. (B8), respectively.

Note also that we may have, e.g., $U_{11} < 0$, $U_{22} > 0$, but $\omega_{1,q}^2 + \omega_{2,q}^2 > 0$ (i.e., $D_{11} + D_{22} > 0$). Such a two-component system can be dynamically stable since $U_{12}^2 > U_{11}U_{22}$.

[1] B. P. Anderson and M. A. Kasevich, Science **282**, 1686 (1998).

[2] S. Burger, F. S. Cataliotti, C. Fort, F. Minardi, M. Inguscio, M. L. Chiofalo, and M. P. Tosi, Phys. Rev. Lett. **86**, 4447 (2001).

[3] O. Morsch, J. H. Müller, M. Cristiani, D. Ciampini, and E. Arimondo, Phys. Rev. Lett. **87**, 140402 (2001).

[4] F. S. Cataliotti, S. Burger, C. Fort, P. Maddaloni, F. Minardi, A. Trombettoni, A. Smerzi, and M. Inguscio, Science **293**, 843 (2001).

[5] F. S. Cataliotti, L. Fallani, F. Ferlaino, C. Fort, P. Maddaloni, and M. Inguscio, New J. Phys. **5**, 71 (2003).

[6] M. Cristiani, O. Morsch, M. Malossi, M. Jona-Lasinio, M. Anderlini, E. Courtade, and E. Arimondo, Opt. Express **12**, 4 (2004).

[7] L. Fallani, L. De Sarlo, J. E. Lye, M. Modugno, R. Saers, C. Fort, and M. Inguscio, Phys. Rev. Lett. **93**, 140406 (2004).

[8] L. De Sarlo, L. Fallani, J. E. Lye, M. Modugno, R. Saers, C. Fort, and M. Inguscio, Phys. Rev. A **72**, 013603 (2005).

[9] C. D. Fertig, K. M. O'Hara, J. H. Huckans, S. L. Rolston, W. D. Phillips, and J. V. Porto, Phys. Rev. Lett. **94**, 120403 (2005).

[10] A. K. Tuchman, W. Li, H. Chien, S. Dettmer, and M. A. Kasevich, New J. Phys. **8**, 311 (2006).

[11] A. J. Ferris, M. J. Davis, R. W. Geursen, P. B. Blakie, and A. C. Wilson, e-print arXiv:0706.2744.

[12] B. Wu and Q. Niu, Phys. Rev. A **64**, 061603(R) (2001).

[13] A. Smerzi, A. Trombettoni, P. G. Kevrekidis, and A. R. Bishop, Phys. Rev. Lett. **89**, 170402 (2002).

[14] B. Wu and Q. Niu, New J. Phys. **5**, 104 (2003).

[15] Y. Zheng, M. Kostrun, and J. Javanainen, Phys. Rev. Lett. **93**, 230401 (2004).

[16] M. Modugno, C. Tozzo, and F. Dalfovo, Phys. Rev. A **70**, 043625 (2004).

[17] A. Polkovnikov and D.-W. Wang, Phys. Rev. Lett. **93**, 070401 (2004).

[18] J. Ruostekoski and L. Isella, Phys. Rev. Lett. **95**, 110403 (2005).

[19] J. Gea-Banacloche, A. M. Rey, G. Pupillo, C. J. Williams, and C. W. Clark, Phys. Rev. A **73**, 013605 (2006).

[20] Note also that, at least in deep lattices, the dissipative atom current, or friction, may manifest itself in the formation of phase slips, as studied by A. Polkovnikov, E. Altman, E. Demler, B. Halperin, and M. D. Lukin, Phys. Rev. A **71**, 063613 (2005).

[21] J. M. Vogels, R. S. Freeland, C. C. Tsai, B. J. Verhaar, and D. J. Heinzen, Phys. Rev. A **61**, 043407 (2000).

[22] D. S. Hall, M. R. Matthews, J. R. Ensher, C. E. Wieman, and E. A. Cornell, Phys. Rev. Lett. **81**, 1539 (1998).

[23] Z. Dutton, M. Budde, C. Slowe, and L. V. Hau, Science **293**, 663 (2001).

[24] H. J. Lewandowski, D. M. Harber, D. L. Whitaker, and E. A. Cornell,Phys. Rev. Lett. **88**, 070403 (2002).

[25] T. Nikuni and J. E. Williams, J. Low Temp. Phys. **133**, 323 (2003).

[26] G. Modugno, M. Modugno, F. Riboli, G. Roati, and M. Inguscio, Phys. Rev. Lett. **89**, 190404 (2002).

[27] A. Sorensen, L.-M. Duan, J. I. Cirac, and P. Zoller, Nature (London) **409**, 63 (2001).

[28] J. Ruostekoski and J. R. Anglin, Phys. Rev. Lett. **86**, 3934 (2001).

[29] Th. Busch and J. R. Anglin, Phys. Rev. Lett. **87**, 010401 (2001).

[30] C. M. Savage and J. Ruostekoski, Phys. Rev. Lett. **91**, 010403 (2003).

[31] O. Mandel, M. Greiner, A. Widera, T. Rom, T. W. Hänsch, and I. Bloch, Nature (London) **425**, 937 (2003).

[32] J. Catani, L. De Sarlo, G. Barontini, F. Minardi, and M. Inguscio, e-print arXiv:0706.2781.

[33] J. Stenger, S. Inouye, D. M. Stamper-Kurn, H. J. Miesner, A. P. Chikkatur, and W. Ketterle, Nature (London) **396**, 345 (1998).

[34] H.-J. Miesner, D. M. Stamper-Kurn, J. Stenger, S. Inouye, A. P. Chikkatur, and W. Ketterle, Phys. Rev. Lett. **82**, 2228 (1999).

[35] A. E. Leanhardt, Y. Shin, D. Kielpinski, D. E. Pritchard, and W. Ketterle, Phys. Rev. Lett. **90**, 140403 (2003).

[36] F. Zhou, Int. J. Mod. Phys. B **17**, 2643 (2003).

[37] J. Ruostekoski and J. R. Anglin, Phys. Rev. Lett. **91**, 190402 (2003).

[38] E. J. Mueller, Phys. Rev. A **69**, 033606 (2004).

[39] J. W. Reijnders, F. J. M. van Lankvelt, K. Schoutens, and N. Read, Phys. Rev. A **69**, 023612 (2004).

[40] H. Schmaljohann, M. Erhard, J. Kronjäger, M. Kottke, S. van Staa, L. Cacciapuoti, J. J. Arlt, K. Bongs, and K. Sengstock, Phys. Rev. Lett. **92**, 040402 (2004).

[41] M.-S. Chang, C. D. Hamley, M. D. Barrett, J. A. Sauer, K. M. Fortier, W. Zhang, L. You, and M. S. Chapman, Phys. Rev. Lett. **92**, 140403 (2004).

[42] J. Kronjäger, C. Becker, M. Brunkmann, R. Walser, P. Navez, K. Bongs, and K. Sengstock, Phys. Rev. A **72**, 063619 (2005).

[43] A. T. Black, E. Gomez, L. D. Turner, S. Jung, and P. D. Lett, Phys. Rev. Lett. **99**, 070403 (2007).

[44] A. Widera, F. Gerbier, S. Fölling, T. Gericke, O. Mandel, and I. Bloch, Phys. Rev. Lett. **95**, 190405 (2005).

[45] M. Vengalattore, J. M. Higbie, S. R. Leslie, J. Guzman, L. E. Sadler, and D. M. Stamper-Kurn, Phys. Rev. Lett. **98**, 200801 (2007).

[46] S. Hooley and K. A. Benedict, Phys. Rev. A **75**, 033621 (2007).

[47] B. J. Dabrowska-Wüster, E. A. Ostrovskaya, T. J. Alexander, and Y. S. Kivshar, Phys. Rev. A **75**, 023617 (2007).

[48] D. M. Harber, H. J. Lewandowski, J. M. McGuirk, and E. A. Cornell, Phys. Rev. A **66**, 053616 (2002).

[49] D. Jaksch, C. Bruder, J. I. Cirac, C. W. Gardiner, and P. Zoller, Phys. Rev. Lett. **81**, 3108 (1998).

[50] C. Pethick and H. Smith, *Bose-Einstein Condensation in Dilute Gases* (Cambridge University Press, Cambridge, U.K., 2002).

[51] A. Widera, F. Gerbier, S. Fölling, T. Gericke, O. Mandel, and I. Bloch, New J. Phys. **8**, 152 (2006).

[52] In principle, an external magnetic field may also induce a different hopping amplitude for different internal levels, but in the present study we ignore such effects.

[53] D. Vollhardt and P. Wölfle, *The Superfluid Phases of Helium 3* (Taylor and Francis, London, 1990).

[54] A. Corney, *Atomic and Laser Spectroscopy* (Oxford University Press, Oxford, 1977).

[55] F. Gerbier, A. Widera, S. Fölling, O. Mandel, and I. Bloch, Phys. Rev. A **73**, 041602 (2006).

[56] The symmetry of the ground state manifold of the polar state Eq. (18) in the absence of the magnetic splitting, $S^1 \times S^2/Z_2$ (where Z_2 denotes a two-element group), is reduced in Eq. (30) to $S^1 \times S^1/Z_2$.

[57] The ^{87}Rb-^{85}Rb mixture exhibits a particularly rich system of interspecies Feshbach resonances [S. J. J. M. F. Kokkelmans (private communication)].

[58] M. Kozuma, L. Deng, E. W. Hagley, J. Wen, R. Lutwak, K. Helmerson, S. L. Rolston, and W. D. Phillips, Phys. Rev. Lett. **82**, 871 (1999).

[59] L. Isella and J. Ruostekoski, Phys. Rev. A **72**, 011601(R) (2005); **74**, 063625 (2006).

[60] J. Ruostekoski, G. V. Dunne, and J. Javanainen, Phys. Rev. Lett. **88**, 180401 (2002).